

## **Chapter 13**

### **Remote Sensing of Precipitation from Airborne and Spaceborne Radar**

S. Joseph Munchak

NASA Goddard Space Flight Center

Greenbelt, MD, USA

#### **Abstract**

Weather radar measurements from airborne or satellite platforms can be an effective remote sensing tool for examining the three-dimensional structures of clouds and precipitation. This chapter describes some fundamental properties of radar measurements and their dependence on the particle size distribution (PSD) and radar frequency. The inverse problem of solving for the vertical profile of PSD from a profile of measured reflectivity is stated as an optimal estimation problem for single- and multi-frequency measurements. Phenomena that can change the measured reflectivity  $Z_m$  from its intrinsic value  $Z_e$ , namely attenuation, non-uniform beam filling, and multiple scattering, are described and mitigation of these effects in the context of the optimal estimation framework is discussed. Finally, some techniques involving the use of passive microwave measurements to further constrain the retrieval of the PSD are presented.

#### **[[H1]] Introduction**

The ability of weather radar to measure the location and intensity of precipitation was rapidly realized in the late 1940s following World War II. However, ground-based radars are limited in their ability to directly detect precipitation close to the ground far from the radar site due to ground clutter, refraction of the radar beam, and the curvature of the earth. Beam blockage by terrain also poses problems for radar coverage in mountainous areas. Coverage over oceans and other remote areas, where maintaining a ground radar would be difficult and costly, is also impractical, yet the precipitation that falls in these regions has important impacts on the global

atmospheric circulations via latent heating (e.g., Hoskins and Karoly, 1981, Hartmann et al., 1984, Matthews et al., 2004) and can have a profound influence on weather patterns thousands of kilometers away. Likewise, knowledge of precipitation over land, particularly in the form of snow, is a crucial component of the mass balance equation for glaciers and ice sheets, which must be properly characterized for realistic climate simulations (Shepherd et al., 2012).

Airborne radar systems can provide high sensitivity and finely resolved vertical profiles to characterize precipitation microphysics for the benefit of model parameterizations and process understanding (e.g., Reinhardt et al, 2010, Heymsfield et al., 2013, Rauber et al., 2016). However, in order to achieve true global coverage, it had been proposed from nearly the beginning of the space age to put a weather radar in space (Kreigler and Kawitz, 1960), and efforts to do so began in earnest in the late 1970s and 1980s with the planning of the Tropical Rainfall Measuring Mission satellite (TRMM; Simpson et al., 1987, Okamoto et al., 1988) with its Ku-band Precipitation Radar (PR; Table 1), which was launched in 1997. TRMM was followed in 2014 by the Global Precipitation Measurement (GPM; Hou et al., 2014) mission with its Ku- and Ka-band Dual-frequency Precipitation Radar (DPR; Table 1), which provides increased accuracy, sensitivity, and extension to higher latitudes. Both the TRMM PR and GPM DPR were intended not only to estimate precipitation directly from the radar data but also to construct a database of precipitation profiles to unify precipitation retrievals from passive microwave radiometers (Hou et al., 2014, Kummerow et al., 2015), enabling more frequent coverage than is possible from a narrow-swath on a single satellite. Meanwhile, in 2006, the CloudSat mission (Stephens et al., 2002) with a W-band Cloud Profiling Radar (CPR; Table 1),

was launched into polar orbit, complementing TRMM and GPM by providing estimates of light precipitation at high latitudes (Behrangi et al., 2014).

<<Table 00-01>> Key parameters of spaceborne weather radars launched prior to 2016. The GPM DPR consists of two radars with matched beams: the KuPR and KaPR.

[begin box]

In radar engineering and meteorology, it is common to refer to specific frequency ranges (bands) by letter designation. This table lists bands commonly used for meteorological radars according to the IEEE Standard 521-2002. Some of these bands contain gas absorption lines, where atmospheric extinction can be orders of magnitude higher than the surrounding “window” regions. However, it has been proposed to use radars operating at two or more closely-spaced frequencies near some of these bands to estimate vertical profiles of water vapor (e.g., Meneghini et al., 2005, Lebsock et al., 2015) by taking advantage of the differential attenuation.

<<Table 00-02>> Band designations, frequency ranges, and significant absorption lines in each band.

[end box]

In order to minimize size and weight, which strongly correspond to the cost of a satellite mission, it is necessary to use higher frequencies (Ku-, Ka-, or W-band) than are typical for ground radar systems. With increasing frequency, power and antenna size requirements for a desired sensitivity and horizontal resolution are reduced, but attenuation and multiple scattering, which can lead to ambiguity in converting reflectivity to precipitation rate, increase. Even at higher frequencies, the distance from low earth orbit results in ground footprints that are large relative to the scale of variability in most precipitation systems and this non-uniformity must also be

considered in precipitation retrieval algorithms. This chapter is intended to provide an overview of the theoretical basis and some practical implementations of precipitation retrieval algorithms for nadir (or near-nadir) looking airborne and spaceborne weather radars at attenuating frequencies, without consideration of polarimetric quantities or Doppler velocity. While dual-polarimetric radars are widely used from ground-based platforms to identify preferentially-oriented, non-spherical hydrometeors, at near-nadir incidence angles these measurements are of limited utility although the linear depolarization ratio measurements can be useful for identifying melting layers and non-spherical ice particles (Pazmany et al., 1994; Galloway et al., 1997). Doppler velocities are useful for inferring hydrometeor fall speeds and at multiple frequencies can be highly effective in discerning cloud liquid from rain (e.g., Kollias et al., 2007) as well as identification of ice particle habits (Kneifel et al., 2016), but obtaining them from rapidly-moving satellite platforms is a difficult engineering challenge that will first be attempted in the EarthCARE mission (Illingworth et al., 2015).

Table 1 – Characteristics of TRMM, GPM, and CloudSat Spaceborne Weather Radars

## **[[H1]] Radar Precipitation Measurement Fundamentals**

The earliest attempts to measure rainfall with radar (Marshall et al., 1947) found that, in general, a power law relationship between radar reflectivity factor  $Z$  and rainfall rate  $R$  existed:

$$Z = aR^b. \tag{1}$$

The coefficient  $a$  and exponent  $b$  of this power law were later provided by Marshall and Palmer (1948), whose values are still in wide use today. Despite this common usage, it was quickly recognized (e.g., Atlas and Chmela 1957) that these parameters varied widely and seemed to be associated with synoptic conditions. It is now recognized (e.g., Brandes et al.,

2006) that the power law of Marshall and Palmer (1948) is more representative of frontal stratiform rainfall, which is the predominant rainfall type in Ontario, Canada where the radar and rainfall observations upon which this power law was based were taken. Convective and tropical rainfall, for example, is observed to have a smaller coefficient  $a$  (Tokay and Short, 1996). A more comprehensive review of varying power law relations is given by Battan (1973). For the purposes of this chapter, is sufficient to recognize that the non-uniqueness of the  $Z$ - $R$  relationship is a fundamental result of the general equations for radar reflectivity and rainfall rate:

$$Z = \int_{D_{min}}^{D_{max}} N(D)D^6 dD, \quad (2)$$

$$R = \frac{\pi}{6} \int_{D_{min}}^{D_{max}} D^3 N(D)V(D)dD, \quad (3)$$

where  $v(D)$  is the drop fall speed. Owing to the fact that vertical air motions are small near the ground and that raindrops achieve terminal fall velocity within about 100m (Section 10.3.6, Pruppacher and Klett, 1997) formulae relating terminal fall speed to drop size are often used. A simple power law such as  $v(D)=17.67D^{0.67}$  (where  $V$  is in  $m s^{-1}$  and  $D$  is in cm; Atlas and Ulbrich, 1977) is convenient for calculation of  $Z$ - $R$  power law coefficients by combining (2) and (3), especially when an analytic form of the drop size distribution  $N(D)$  is assumed. Slightly more accurate piecewise power laws such as the one given by Beard (1976) account for different hydrodynamic regimes as drops grow in size, and this is the relationship used for all rain rate calculations in this chapter.

In (2), there is no dependence of  $Z$  on the radar wavelength. This is only valid when the particle size is much smaller than the wavelength. For larger sizes, the equivalent reflectivity factor  $Z_e$  is used instead:

$$Z_e = \frac{\lambda^4}{\pi^5 |K|^2} \int_{D_{min}}^{D_{max}} N(D)\sigma_b(D, \lambda)dD, \quad (4)$$

where  $K$  is a function of the complex index of refraction,  $\lambda$  is the radar wavelength in mm,  $\sigma_b$  is the backscattering cross section (in  $\text{mm}^2$ ), and  $N(D)$  is the number concentration of raindrops (in  $\text{m}^{-3}$ ) per size interval, resulting in units of  $\text{mm}^6\text{m}^{-3}$  for  $Z_e$ . Note that (3) and (4) are also valid for frozen and melting particles, however, the definition of particle size (and fall speeds) becomes ambiguous for non-spherical particles, and even large raindrops exhibit some departures from sphericity. For the remainder of this chapter, the convention will be that  $D$  represents the diameter of an equal-mass homogeneous (solid or liquid) sphere, so that  $N(D)$  is equivalent to a mass distribution, and  $N(D)$  will be referred to as the particle size distribution (PSD).

The backscattering cross section describes the amount of electromagnetic radiation that is scattered towards the source of incident radiation. For particles much smaller than the wavelength, the individual dipoles that comprise the particle can be treated as coherent scatterers, and the Rayleigh approximation holds:

$$\sigma_b = \frac{\pi^5 |K|^2 D^6}{\lambda^4} \quad (5)$$

and (4) becomes (2). As the size parameter  $\pi D/\lambda$  approaches one, the Rayleigh approximation breaks down and Mie theory, which provides exact results for spheres, should be used.. For particles that are rotationally symmetric about one axis (such as oblate or prolate spheroids, cylinders, or cones),  $\sigma_b$  can be calculated from the T-Matrix (Mishchenko and Travis, 1998). Finally,  $\sigma_b$  for arbitrarily-shaped particles can be calculated with the discrete-dipole approximation (Draine and Flatau, 1994), a method often used for realistically-shaped snowflakes (e.g., Liu (2004), Kim (2006), Petty and Huang (2010), Kwo et al. (2016)) and melting particles (Johnson et al., 2016). Plots of  $\sigma_b$  from all of these approximations can be

found in Figure 1 for spherical and oblate raindrops and spherical, cylindrical, and synthetically-grown ice particles and aggregates.

<<Figure 1: Backscattering efficiencies calculated at Ku-, Ka-, and W-band frequencies for rain and ice particles. Spheroidal raindrops were modeled according to aspect ratio and canting angle distributions given in Beard et al., 2010. The cylindrical snow particles, which are an effective representation of hexagonal plates (Adams et al., 2012), were modeled with an aspect ratio ( $D/h$ ) = 6 and effective density of  $0.6 \text{ g/cm}^3$ . The DDSCAT particles (color indicates relative density) are from the database of Kwo et al. (2016). >>

Although the departures of reflectivity from Rayleigh theory are important, particularly for multi-frequency radars, it is still the case that while  $Z$  is approximately proportional to the 6<sup>th</sup> moment of the DSD, rain rate is proportional to a much lower 3.67<sup>th</sup> moment. This is illustrated in Figure 2, which shows the relative contribution of different drop sizes to reflectivity and rain rate for a typical exponential DSD. Thus the fundamental problem in radar meteorology is that multiple values of  $R$  can be associated with a single value of  $Z$ .

<<Figure 2: Relative contribution (in 0.1 mm bins) to reflectivity ( $Z$ ) and rainfall rate ( $R$ ) of an exponential drop size distribution with a median volume-weighted diameter of 1.5 mm. >>

Aside from backscatter, another characteristic of precipitation particles that is critical for understanding radar measurements is the extinction cross-section  $\sigma_e$ . This quantity describes the amount of electromagnetic radiation absorbed and scattered by the particle, and like  $\sigma_b$  depends on the dielectric constant, particle size, and shape (for size parameters close to or greater than one). Figure 3 shows the extinction efficiency for the same particle types in Figure 1.

<<Figure 3: Extinction efficiencies calculated at Ku-, Ka-, and W-band frequencies for rain and ice particles. Particle type description can be found in the Figure 1 caption.>>

For particles with small size parameters,  $\sigma_e$  is given by:

$$\sigma_e = \frac{\pi^2 D^3}{\lambda} \Im\left(\frac{m^2-1}{m^2+2}\right), \quad (6)$$

where  $m$  is the complex index of refraction and  $\Im(x)$  denotes the imaginary part of  $x$ . The bulk extinction coefficient,  $k_{ext}$ , can be calculated by integrating  $\sigma_e$  over the particle size distribution:

$$k_{ext} = \int_{D_{min}}^{D_{max}} \sigma_e N(D) dD. \quad (7)$$

Note that in addition to precipitation particles, atmospheric gases such as oxygen and water vapor can have non-negligible contributions to  $k_{ext}$  at some wavelengths common to airborne and spaceborne radars (Li et al., 2001; Tanelli et al., 2006, Ellis and Vivekanandan, 2010). Cloud water, which has a negligible contribution to radar reflectivity at Ka-band and lower frequencies, nevertheless can contribute significantly to  $k_{ext}$  at these frequencies as well (Grecu and Olson, 2008). Note the independence of  $k_{ext}$  with respect to  $D_m$  in the limit of small  $D_m$  in Figure 5. This follows from (6) and shows that in the limit of small particles,  $k_{ext}$  is directly proportional to the water/ice content. The effect of bulk extinction on the measured reflectivity can be calculated by integrating  $k_{ext}$  along the two-way radar propagation path:

$$Z_m(r) = e^{-0.21 \ln(10) \int_0^r k_{ext}(s) ds} Z_e(r) \quad (8)$$

Note that while  $Z_e$  is an intrinsic property of the PSD at a given location,  $Z_m$  also depends on the integrated bulk extinction between the source of the radar signal and that location, creating another source of uncertainty when converting from  $Z$  to  $R$ . Therefore, understanding the vertical profile of the PSD, on which  $Z$ ,  $k_{ext}$ , and  $R$  depend, is fundamental to the radar-precipitation profiling algorithms that are described in this chapter.

## [[H1]] The Particle Size Distribution

The previous section demonstrated that knowledge of the particle size distribution (PSD) is needed to convert  $Z$  to the physical integrated quantities such as precipitation rate  $R$  and water content  $W$ . It is often convenient to assume an analytical form of the PSD that describes the shape with a few (relative to a discrete bin representation) free parameters. Although PSD models with as many as eight free parameters have been proposed (Kuo et al., 2004), most often the modified gamma distribution with three free parameters (Ulbrich, 1983) is used:

$$N(D) = N_0 D^\mu \exp(-\Lambda D). \quad (9)$$

The free parameters are often referred to as the intercept ( $N_0$ ), slope ( $\Lambda$ ), and shape ( $\mu$ ). These names describe the mathematical form of the distribution more so than physical quantities, and it is difficult to impart any physical meaning to a value for anyone one of the parameters given in isolation. However, it is possible to re-cast these parameters in terms of physical quantities through the following relationships (Testud et al., 2001; Williams et al., 2014):

$$D_m = \frac{4+\mu}{\Lambda}, \quad (10)$$

$$N_w = N_0 D_m^\mu \frac{\Gamma(4+\mu)}{\Gamma(4)} \frac{256}{(4+\mu)^{4+\mu}}, \quad (11)$$

$$\sigma_m = \frac{D_m}{\sqrt{4+\mu}}, \quad (12)$$

where  $D_m$  is the mass-weighted mean diameter (also defined as the ratio of the 4<sup>th</sup> to 3<sup>rd</sup> moment of the PSD),  $N_w$  is the normalized intercept parameter defined such that it is equal to  $N_0$  for an exponential ( $\mu=0$ ) PSD of the same water content and  $D_m$  (Bringi and Chandrasekhar 2001), and  $\sigma_m$  is the mass spectrum standard deviation. The median volume diameter,  $D_0$ , describes the particle size such that  $\int_{D_{min}}^{D_0} D^3 dD = \int_{D_0}^{D_{max}} D^3 dD$ , and for a gamma distribution  $D_0 =$

$\frac{3.67+\mu}{4+\mu} D_m$ . Note that these expressions are only valid for a PSD where particle density is constant

with size. For realistic frozen particles, this is often not the case, and formulae to convert PSD parameters from observed to solid-sphere-equivalent particle sizes can be found in Petty and Huang (2011).

Analysis of disdrometer observations has shown that neither the three free parameters in (9) nor the physical quantities in (10)-(12) are statistically independent in rain (e.g., Haddad et al., 1996; Zhang et al., 2003; Munchak and Tokay, 2008; Williams et al., 2014.) and relationships between the parameters can be formulated to reduce the degrees of freedom in (9). This is particularly useful for radar precipitation retrieval algorithms because it allows for a common basis from which to compute  $Z$ - $R$  and  $Z$ - $k_{ext}$  relationships, and, when joint probability distribution functions (pdfs) of PSD parameters are known, these *a priori* statistics can be used to constrain the retrieval of PSD parameters from radar profiles of reflectivity and other information.

To demonstrate the relationship between PSD parameters and radar reflectivity  $Z$ , Figures 4 and 5 show reflectivity and extinction coefficients integrated over PSDs with  $D_m$  ranging from 0.1 to 3 mm and  $\mu$  ranging from -1 to 3 for snow and following the  $\sigma_m$ - $D_m$  relationships given by Williams et al. (2014) for rain. The integrated water content of all PSDs was normalized to  $W=1$  g m<sup>-3</sup> to emphasize the importance of the shape of the PSD in terms of its mean and dispersion on the reflectivity and extinction. For these PSDs, the equivalent intercept  $N_w$  can be calculated from  $D_m$  and  $W$  (Testud et al., 2001):

$$N_w = \frac{256}{\pi \rho_w} \frac{W}{D_m^4}. \quad (13)$$

<<Figure 4: Reflectivity for rain and ice PSDs at Ku-, Ka-, and W-band as a function of mass-weighted mean particle diameter  $D_m$  for various shape parameter assumptions. All PSDs contain  $1 \text{ g m}^{-3}$  of water content.>>

<<Figure 5: Bulk extinction coefficient at Ku-, Ka-, and W-band for the same PSDs represented in Figure 4.>>

While analytic expressions relating  $Z$ ,  $D_m$ ,  $W$ , and  $R$  can be derived from the gamma distribution (Ulbrich and Atlas, 1998), statistical relationships can also be derived directly from disdrometer measurements without any assumptions of the PSD shape. In Figure 6, scatter plots of  $k_{ext}$ ,  $W$ ,  $R$ ,  $D_m$ , and  $N_w$  versus  $Z$  at Ku-band are shown for rain PSDs measured during the IFloodS field experiment (Ryu et al., 2016). Most of these parameters (except  $N_w$ ) have a strong correlation to reflectivity. As will be shown later in this chapter, it is particularly useful for radar-based precipitation retrievals to modify a parameter that is uncorrelated to reflectivity, and measurements from IFloodS and other field experiments suggest that  $N_w$  is a strong candidate for such a parameter. However, any integral parameter may be transformed to one that is uncorrelated with reflectivity by deriving a reflectivity power law relationship (such as equation 1) and converting a to ‘normalized’ quantities  $k'$ ,  $W'$ ,  $R'$ ,  $D_m'$ , and  $N_w'$ , e.g. (for  $R$ ):

$$R' = \frac{R}{aZ^b}. \quad (14)$$

The correlation plots and coefficients between the normalized parameters are shown in Figure 7. Each panel shows the correlation between a pair of normalized parameters, and it is notable that the squared correlation coefficients are large, in many cases over 0.8. This has strong implications for radar retrievals because it implies that, for a given  $Z$ , if a normalized parameter

such as  $W'$ ,  $D_m'$ ,  $N_w'$  (or just  $N_w$ ), is known, then the other integral parameters, including attenuation, can be predicted to a high degree of accuracy.

<<Figure 6: Ku-band reflectivity power laws and squared correlation coefficient derived from Parsivel<sup>2</sup> disdrometer measurements in Iowa during the IFloodS field experiment for the integral parameters: attenuation coefficient at Ku-band ( $k_{ext}$ ), liquid water content ( $W$ ), rain rate ( $R$ ), mean mass-weighted diameter ( $D_m$ ), and normalized intercept parameter ( $N_w$ ). >>

<<Figure 7: Scatter diagrams for pairs of normalized integral quantities (equation 14) from the IFloodS disdrometer measurements. The squared logarithmic correlation coefficient is labeled in each panel. >>

### [[H1]] Single-Frequency Methods

Since many airborne and spaceborne radars operate at frequencies where attenuation by rain is significant, a correction for this attenuation must be made. A radar algorithm that corrects for attenuation was first described by Hitschfeld and Bordan (1954). If a  $Z$ - $k_{ext}$  power law of the form

$$k_{ext} = \alpha Z_e^\beta, \quad (15)$$

and  $\beta$  is constant with respect to range, then the path-integrated attenuation (PIA), which is the integral in the exponential term of (8), can be solved for analytically:

$$PIA(r) = \frac{-1}{0.1 \ln(10) \beta} \ln(1 - 0.2 \ln(10) \beta \int_0^r \alpha(s) Z_m^\beta(s) ds). \quad (16)$$

However, this method is numerically unstable because small changes in the  $Z$ - $k_{ext}$  relationship can lead to large changes in path-integrated attenuation (PIA) at far range gates. This can be inferred from (15) if the values of  $\alpha$ ,  $\beta$ , and  $Z_m$  are such that the argument of the logarithm is near

or less than zero, in which case the PIA is undefined. An example, illustrated in Figure 6, provides a physical interpretation of how linear increases in  $\alpha$  lead to nonlinear increases in PIA. In physical terms, if the estimated attenuation is too large at a given range gate, then attenuation-corrected reflectivities will be overestimated in subsequent range gates. These overestimated reflectivities will produce an even larger attenuation correction in further range gates, which will result in reflectivity and attenuation estimates that can increase to unphysical values.

<<Figure 8: An example attenuation-correcting radar profiling algorithm. The true effective reflectivity (solid) is attenuated to the measured signal (dashed). An attenuation correction is applied assuming  $Z-k$  relationships that have been multiplied by factors ranging from 0.5 to 1.5.>>

While attenuation is a potential source of error if not accurately corrected, it can also be an additional source of information. Equation 8 includes a term describing the PIA. If a reflector of known effective cross section is placed at the end of the path, then the apparent decrease in this cross section from its known value is equal to the PIA. Fortunately, a downward-looking radar has exactly such a reference cross section in the earth's surface itself. This fact was recognized by Meneghini et al. (1983) and forms the fundamental basis for the Surface Reference Technique (SRT).

[begin box]

The Surface Reference Technique is a method for obtaining an estimate of the path-integrated attenuation from a downward-looking radar that is independent of the reflectivity profile.

Variations of this method have been used to obtain PIA estimates for use in the TRMM rain-profiling algorithm (Meneghini et al. ,2000), CloudSat's rain profile product (Haynes et al.,

2009; Mitrescu et al., 2010, Lebsock et al., 2011), GPM DPR products (Meneghini et al., 2015), as well as from airborne radars (Tanelli et al., 2006).

The SRT requires a reference value for the normalized surface backscatter cross-section ( $\sigma_0$ ) that is unattenuated by precipitation. Then, the PIA can be calculated by taking the difference of the observed  $\sigma_0$  (in dB units) from the reference:

$$PIA = \sigma_{0,NR} - \sigma_{0,R}. \quad (17)$$

The key to this process is obtaining an accurate estimate of the unattenuated cross-section  $\sigma_{0,NR}$ . In practice, methods for obtaining this reference value include the along-track, across-track, temporal, and geophysical model function. The along-track reference is particularly useful because  $\sigma_0$  varies strongly with incidence angle, thus  $\sigma_{0,NR}$  can be estimated by averaging  $\sigma_0$  in precipitation-free observations surrounding a precipitation observation at the same incidence angle. In the event that a precipitation feature happens to be long in the along-track direction but narrow in the cross-track direction, it may be preferable to use the cross-track reference. In this case, a quadratic function is fit to the precipitation-free  $\sigma_0$  observations to obtain estimates of  $\sigma_{0,NR}$  and PIA in the precipitation feature. The along-track and cross-track spatial methods are most applicable when the surface type does not vary from the region where  $\sigma_{0,NR}$  estimates into the precipitation feature. This can be true over ocean surfaces, but over land or mixed water-land surfaces,  $\sigma_{0,NR}$  can be highly variable, adding considerable uncertainty to the PIA estimate and often producing unphysically negative PIA values. In these cases, the temporal reference can be used. The temporal reference is a gridded average of  $\sigma_{0,NR}$  and its standard deviation over multiple previous observations. In order to minimize the standard deviation of  $\sigma_{0,NR}$ , thus providing more accurate PIA estimates, it is necessary to reduce the grid size to a size approaching the radar footprint (Meneghini and Jones, 2011). However, this is a challenge for

spaceborne radars without a repeating ground track because the number of samples in such a small grid cell at each incidence angle can be small and therefore not representative of changing surface conditions. Meneghini and Kim (2016) suggest optimally including neighboring grid cells in the  $\sigma_{0,NR}$  calculation such that the standard deviation of  $\sigma_{0,NR}$  is minimized.

An alternate method for calculation  $\sigma_{0,NR}$  is the use of a geophysical model function (GMF). This method treats  $\sigma_{0,NR}$  as a function of physical parameters. In general,  $\sigma_0$  depends on the earth incidence angle, surface roughness, and dielectric constant. Over ocean surfaces,  $\sigma_0$  can be largely explained by the surface wind speed and direction (relative azimuth to the radar look angle) and incidence angle (Li et al., 2002; Frielich and Vanhoff, 2003; Munchak et al., 2016). Over land surfaces, no such simple relationships exist but the behavior of  $\sigma_0$  has been found to vary as a function of roughness, soil moisture, and vegetation coverage (Stephen et al., 2010; Puri et al., 2011). The advantage of using a GMF is that the representativeness of the spatial or temporal reference is not an issue; however, the GMF must be well-calibrated, and a source for the physical parameters is required, which itself introduces some uncertainty even for a theoretically perfect GMF. Finally, there is the effect of precipitation on the surface itself (Iguchi and Seto, 2007), which by definition cannot be accounted for by the spatial or temporal references but could be included in a GMF.

Another innovative technique which is made possible with a dual-frequency radar is the dual-frequency SRT (dSRT; Meneghini et al., 2012). This technique determines the differential PIA at two frequencies by taking a difference of differences from (16). If there is a positive correlation between  $\sigma_{0,NR}$  at the two frequencies in the reference dataset, which is often the case, then the error in the differential PIA will be reduced from the single-frequency error using the same reference data. Regardless of the source for the surface reference, it is critical that it can also

provide an estimate of the standard deviation of  $\sigma_{0,NR}$ , which from (16) can be considered to be the standard deviation of the PIA. The larger the PIA is relative to this standard deviation, the more useful it is to constrain the precipitation PSD via the  $Z-k_{ext}$  relationship.

[end box]

With an independent estimate of the PIA, it is possible to constrain the precipitation profiles to those that produce the same or similar PIA, given the uncertainty that comes from the SRT. The observed profile of  $Z_m$ , in conjunction with a vertical profile model of the  $Z-k_{ext}$  relationships, can be used to apportion the PIA vertically. As shown earlier in this chapter (Figures 4 and 5), the  $Z-k_{ext}$  relationships depend on the PSD and precipitation phase, and so by modifying the  $Z-k_{ext}$  relationship to produce a profile that matches the SRT PIA, the PSD is also implicitly modified. The vertical profile model is also used to extend the PSD into the range gates near the surface that are contaminated by ground clutter. This layer can be 1km deep or more for a spaceborne radar depending on the beam width, pulse width, and incidence angle (Takahashi et al., 2016), and presents a difficulty in obtaining precipitation rates for shallow clouds either by failing to detect them entirely or by missing much of the growth of rain drops if it occurs within the clutter-affected gates (Shimizu et al., 2009). Sidelobe clutter presents a more severe problem in that it can contaminate range gates far from the surface at off-nadir angles. A thorough description of sidelobe clutter mitigation techniques for the GPM DPR is given by Kubota et al., 2016. Returning to the nomenclature in (14), and assuming that the normalized PSD parameter is constant in the vertical (implying that all vertical variability is represented by  $Z$ ),  $k'$  can be inserted into (16) as a multiplier to  $\alpha$ , and a value for  $k'$  can be obtained that exactly matches the observed PIA. However, because there is always some uncertainty in the SRT PIA (which may even be negative in some cases), and very large or small values of  $k'$  may imply unphysical

PSDs, it is valuable to derive a solution that considers both the error characteristics of the PIA and prior knowledge of the joint pdfs of PSD parameters (Figure 7). With this knowledge, a maximum likelihood estimate can be found along with a pdf of solutions to the observed radar profile. Various PSD models and vertical profile models have been applied to TRMM (Iguchi et al., 2000, 2009), GPM (Seto et al., 2015), CloudSat (L'Ecuyer and Stephens, 2002, Mitrescu et al., 2010), and airborne radar (Amayenc et al., 1996, Grecu et al., 2011) data in some form of a probabilistic framework.

In a general form, probabilistic, or optimal estimation, retrieval frameworks seek to minimize an objective function of the form:

$$J = (\mathbf{y} - f(\mathbf{x}))^T \mathbf{S}_y^{-1} (\mathbf{y} - f(\mathbf{x})) + (\mathbf{x} - \mathbf{x}_a)^T \mathbf{S}_a^{-1} (\mathbf{x} - \mathbf{x}_a), \quad (18)$$

where  $\mathbf{y}$  is the observation vector,  $\mathbf{x}$  is the retrieval parameter (or state) vector,  $f(\mathbf{x})$  is the forward model,  $\mathbf{x}_a$  is the a priori state vector,  $\mathbf{S}_y$  is the observation and model error covariance matrix, and  $\mathbf{S}_a$  is the state error covariance matrix. Methods of finding the minimum of such objective functions include Gauss-Newton iterative minimization (Rodgers, 2000, Boukabara et al., 2011) and ensemble filter approaches (Eversen, 2006, Grecu et al., 2016). For the radar retrieval problem,  $\mathbf{y}$  may be broadly defined as a set of observed reflectivities  $Z_m$  along a ray or even in three-dimensional space. Likewise,  $\mathbf{x}$  can consist of multiple PSD parameters at each range gate. However, since single-frequency radar retrievals are underconstrained with respect to multiple PSD parameters, it is often more efficient to consider only a single column at a time and include to  $Z_m$  in the forward model, so that  $\mathbf{y}$  contains only the PIA and  $\mathbf{x}$  is reduced to a normalized parameter of the PSD (such as the  $k'$ ,  $D_m'$ ,  $W'$ ,  $R'$ , or  $N_w'$  shown in Figure 7). Implicit in this formulation is that the vertical behavior of the normalized PSD parameter is constant. Owing to the difficulty in making direct measurements of the PSD instantaneously over a vertical column,

such an assumption is difficult to verify. Analyses of measurements made with multi-parameter radars (Bringi et al., 2016) and profilers (Williams, 2016) suggest that the vertical decorrelation lengths of normalized PSD parameters are on the same order as the vertical extent of precipitation, implying that, absent any other measurements, the column-averaged normalized PSD parameter should be representative of the surface value.

In summary, the fundamental process of converting from a vertical profile of radar reflectivity to precipitation physical parameters is the correction of attenuation via a vertical profile model of the PSD and associated  $Z-k_{ext}$  relationships, and making adjustments to this model to achieve agreement with independent estimates of the PIA. The equations and assumptions presented so far are valid for uniform beam filling and no multiple scattering, which can greatly impact SRT PIA,  $Z-k_{ext}$ , and  $Z-R$  relationships. These issues will be discussed later in this chapter.

### **[[H1]] Multi-Frequency Methods**

The frequency dependence of backscattering efficiency (when size parameter becomes similar to the wavelength) and extinction efficiency have motivated the development of radar systems operating at two or more frequencies (e.g., Sadowy et al., 2003, Li et al., 2008) or separate radars with matched beams (e.g., Chandrasekhar et al., 2010, Battaglia et al., 2016) so that these differences can be used to further constrain the range-resolved parameters of the PSD. For any pair of frequencies  $\nu_1$  and  $\nu_2$ , where  $\nu_1 < \nu_2$ , the dual-frequency ratio (DFR) is defined as:

$$DFR = 10 \log_{10} \left( \frac{Z_1}{Z_2} \right) = dBZ_1 - dBZ_2. \quad (19)$$

When a gamma distribution PSD is assumed (9), and the equation for effective reflectivity (4) is inserted into (19), the DFR has the convenient property of only depending on the shape and slope (or alternatively,  $D_m$  and  $\sigma_m$ ) parameters of the gamma PSD. In principle, then, it is possible to

retrieve  $D_m$  from the DFR (after attenuation correction has been performed) and an assumption regarding  $\mu$ , such as a constant value (Liao et al., 2014), reflectivity-dependent value (Munchak and Tokay 2008),  $\mu$ - $A$  relationship (Zhang et al., 2003), or  $\sigma_m$ - $D_m$  relationship (Williams et al., 2014). At some frequency pairs, such as Ku-Ka, there is an ambiguity in that two values of  $D_m$  can be associated with the same DFR for a given  $\mu$  (Figure 9). In these cases, a probabilistic framework and additional observations (such as PIA) can be useful to determine which of these solutions is a better fit to all of the measurements. When the size parameter is small compared to both wavelengths, DFR will be close to zero and invariant with size, necessitating higher frequencies or differential attenuation to determine the PSD parameters.

<<Figure 9: Dual-frequency ratio vs.  $D_m$  for Ku-Ka (left) and Ka-W (right) frequency pairs. Different values for  $\mu$  (ice) or  $\sigma_m$ ' (rain) are indicated by different shades of each color, as in Figures 4 and 5.>>

The impact of adding a frequency on improving the accuracy of the retrieved rainfall rate can be examined with the IFloodS disdrometer dataset. Figure 10 shows the output of a simple Bayesian retrieval using different frequencies individually and in combination. This framework predicts the rainfall rate based on a weighted average of all rainfall rates in the database, where the weights are based on the difference between observed reflectivity and reflectivity at  $n$  frequencies (divided by the measurement error  $\sigma_n$ ) in the database:

$$R_i = \frac{\sum_j R_j w_j}{\sum_j w_j}, \quad (20)$$

where

$$w_j = \exp\left(-\sum_n \frac{(Z_{n,i} - Z_{n,j})^2}{\sigma_n^2}\right). \quad (21)$$

Although the exact values in Figure 10 should not be considered representative of all precipitation regimes, and represent the ideal case (perfect attenuation correction, no multiple scattering or nonuniform beam filling), the impact of additional frequencies is clear in the improved correlation and reduced relative error. It is also apparent that little additional information is provided by extra frequencies at very low rainfall rates, where backscattering follows the Rayleigh approximation for Ku, Ka, and W band.

<<Figure 10: Observed vs. predicted rainfall rate from equation (20) from the IFloodS PSD database for different combinations of Ku, Ka, and W-band reflectivity measurements, assuming a perfect attenuation correction is made and 1 dB measurement error. The squared correlation coefficient ( $r^2$ ) and mean relative error (mre) are given for each combination.>>

Multiple-frequency measurements are also particularly useful in the melting layer and ice phase of precipitation. Le and Chandrasekhar (2013) describe a method to identify the melting layer via the measured (non-attenuation-corrected) DFR. According to this method, the top of the melting layer is at a peak in the slope ( $-dDFR/dZ$ ), a DFR peak occurs within the melting layer due to Mie scattering by large aggregates, and as these collapse into raindrops a local minimum in the DFR signifies the bottom of the melting layer before differential attenuation begins to increase in the rain layer. Within the ice phase, multi-frequency measurements are useful not only for determining mean particle size, but with three frequencies some indication of particle shape can also be discerned (Leinonen et al., 2012; Kulie et al., 2014; Kneifel et al., 2015). The basis for this can be seen when the DFR curves in Figure 9 are plotted against each other in Ku-Ka vs. Ka-W space (Figure 11). In these scattering models, for example, aggregates have much larger Ka-W DFR than pristine plates. Leinonen and Szyrmer (2015) also found that rimed particles tend to have a lower Ka-W DFR for a given Ku-Ka DFR than non-rimed aggregates.

How can the ample information provided by radar measurements at multiple frequencies be incorporated into the probabilistic estimation framework (18)? Because actual reflectivity measurements are noisy, and attenuation in even moderate rainfall can be enough to overwhelm the PSD effect on DFR, strict bin-by-bin PSD retrievals and attenuation correction can be error-prone. One approach to mitigate these errors formulated by Grecu et al. (2011) is to assign only the higher-frequency reflectivities to the observation vector  $\mathbf{y}$  and retrieve  $n-1$  range-resolved PSD parameters in  $\mathbf{x}$ , where  $n$  is the number of radar frequencies. This range-resolved parameter should be independent of  $Z$  ( $N_w$  or a ‘normalized’ PSD parameter such as  $D_m$  are good candidates) and should have a vertical constraint imposed, either via positive off-diagonal values in  $\mathbf{S}_a$  or by retrieving this parameter at a reduced set of nodes within the profile and interpolating values between the nodes. Then, the forward model calculates the profile of  $Z_m$  at the higher frequency from a PSD that matches the lower-frequency reflectivity. PIA at multiple frequencies can also be included in the observation vector, or if the dSRT is used to reduce noise, the difference in PIA can be obtained from the forward model instead.

As with the single-frequency methods, under some circumstances multiple frequency methods can be prone to error if the forward model does not account for non-uniform beam filling and multiple scattering. These phenomena will be discussed in subsequent sections.

### **[[H1]] Effects of non-uniform beam filling**

So far, it has been assumed that the PSD is uniform throughout a radar range gate, and thus the integral parameters such as  $Z$ ,  $R$ , and  $k_{ext}$  do not depend on the horizontal resolution of the radar. Strictly speaking, it is questionable whether “uniform” PSDs exist in nature (Jameson and Kostinksi, 2001), and analyses with networks of disdrometers reveal spatial variability on sub-

100m scales (e.g., Jameson et al., 2015). Practically, any nonuniformity will result in error when  $Z$ - $R$  and  $Z$ - $k_{ext}$  power laws are used to correct for attenuation and retrieve rainfall. As shown by Iguchi et al. (2000, 2009), even if everywhere in a volume,  $R=aZ^b$  is strictly followed, if  $Z$  is not uniform within the volume then the volume mean value of  $R$  will be less than that implied by the volume mean value of  $Z$ :

$$\bar{R} = \overline{aZ_e^b} \leq a\overline{Z_e}^b, \quad (22)$$

because  $b$  is less than one, following Jensen's inequality. Likewise, because the exponent in the  $Z$ - $k_{ext}$  relationships is also less than one,  $k_{ext}$  will also have a low bias relative to the true volume mean. This has further implications for the conversion of  $Z_m$  to  $Z_e$  and the interpretation of the SRT PIA. At any range gate, the measured reflectivity will be the average of the attenuated reflectivities, with the attenuation summed along each infinitesimally narrow pencil beam direction  $(\theta_i, \phi_i)$ , weighted by the antenna gain pattern;

$$Z_m(r) = \overline{Z_e(r, \theta_i, \phi_i)PIA(r, \theta_i, \phi_i)}. \quad (23)$$

The Chebyshev sum inequality for two ordered pairs, which states that if  $a_1 \leq a_2 \leq \dots \leq a_n$  and  $b_1 \geq b_2 \geq \dots \geq b_n$ , then  $\overline{ab} \leq \bar{a}\bar{b}$ , can be used in this context if we let  $a$  represent  $Z_e(r, \theta_i, \phi_i)$  and  $b$  represent the pencil-beam  $PIA(r, \theta_i, \phi_i)$ . If  $Z_e$  and  $PIA$  are ordered accordingly within a radar footprint, then it follows that

$$Z_m \leq \overline{(Z_e)}\overline{(PIA)} \quad (24)$$

Thus the effective attenuation, that is,  $Z_m/Z_e$ , is less than or equal to the SRT PIA (assuming a uniform surface backscatter cross section within the radar field-of-view) if the Chebyshev condition is met.

To further illustrate the effects of nonuniform beam filling (NUBF), two scenarios will be considered: one in which each range gate is composed of varying proportions of empty space and

a uniform PSD, and one in which the shape of the PSD ( $D_m, \mu$ ) is constant but the concentration follows a lognormal distribution within each range gate. An analysis of high-resolution airborne data convolved to lower-resolution satellite footprints by Tanelli et al. (2012) found that these two scenarios fit the vast majority of observations.

For the first scenario, the effect of NUBF on the measurements and retrievals are illustrated in Figure 12 for the sample profile shown in Figure 8. The fraction of beam containing precipitation was varied from 10% to 100% while scaling the PSD such that the column-averaged  $Z_e$  and  $R$  are equal to the uniform case. The measured reflectivity near the surface increases from the uniform case as precipitation fraction decreases as long as the vertical autocorrelation is not high. This is because the PIA along each pencil beam is more evenly distributed than  $Z_e$  at any given level. When the profiles become highly vertically correlated, the attenuation is able to reach higher values and  $\overline{Z_m}$  is reduced from the uniform case. Regardless of the precipitation fraction or vertical correlation structure, the SRT PIA is always reduced from the uniform case. This can be inferred from the beam-integrated equation for the normalized surface backscatter cross section:

$$\sigma_{0,R} = \iint \sigma_{0,NR}(r, \theta) e^{-0.1 \ln(10) PIA(r, \theta)} dr d\theta. \quad (25)$$

If  $\sigma_{0,NR}$  is constant, then the reduction in  $\sigma_{0,R}$  (in dB units) is equal to

$$PIA_{SRT} = 10 \log_{10} \left( \overline{e^{-0.1 \ln(10) PIA(r, \theta)}} \right) \leq \overline{PIA(r, \theta)}. \quad (26)$$

by Jensen's inequality. The reduction is most severe as precipitation fraction decreases and vertical correlation increases, effectively exposing more unattenuated surface, which dominates the measured  $\sigma_0$ .

When a Hitchfeld-Bordan attenuation correction is applied to these profiles under the assumption of uniform beam filling and no adjustment to the intrinsic  $Z-k$  and  $Z-R$  relationships to match the PIA, the errors in  $Z_e$  and  $R$  near the surface correspond to the difference in  $Z_m$  near the surface

compared to the uniform case. When the SRT PIA is used to adjust the  $Z$ - $k$  and  $Z$ - $R$  relationships,  $Z_e$  and  $R$  are biased low due to the low bias of the SRT PIA when NUBF occurs.

<<Figure 12: Non-uniform beam filling scenarios for the  $Z_e$  profile presented in Figure 8. These scenarios vary the fraction of the beam containing precipitation at each level on the vertical axis and the autocorrelation of precipitation from one vertical level to the next on the horizontal axis. In these scenarios, the precipitation is uniform where present and scaled such that the average non-attenuated reflectivity is constant at each level. The difference in measured reflectivity from a uniform beam, SRT PIA, and errors in corrected reflectivity and retrieved rainfall rate near the surface (using default relationships and the SRT PIA to adjust the PSD) are shown.>>

The same set of plots for the second scenario, a filled beam with lognormally-varying  $Z_e$ , is shown in Figure 13. The behavior with respect to the standard deviation of  $dBZ_e$  is similar to the behavior with respect to precipitation fraction in the first scenario, although reversed in sign (with larger  $dBZ_e$  variability corresponding to smaller precipitation fractions). The behavior with respect to vertical correlation structure is also similar, except that the reduction in reflectivity and SRT PIA occurs only when the precipitation structure is almost perfectly aligned with the radar look vector. When the standard deviation of  $dBZ_e$  is only a few dB, the errors from the H-B algorithm are small when the SRT PIA is used, but increase for large variability of  $dBZ_e$  and very large or small vertical autocorrelation. The bias of the unmodified Hitschfeld-Bordan retrieval is closer to zero in these examples, but it must be remembered that variability in the  $Z$ - $k$  relationship was not considered when generating the synthetic profiles, which would add additional random error to the Hitchfeld-Bordan results.

The cases presented in Figures 12 and 13 are not meant to be a universal guide to NUBF biases, since such a guide would require analysis of several different profile shapes, patterns of

nonuniformity, and PSD perturbations. These examples do serve to illustrate the mechanics of NUBF and its dependence on the structure of the horizontal and vertical variability. Although a low bias in the SRT PIA relative to the effective PIA was always present in these examples, one can imagine a scenario where this is not the case. If a beam is slanted with respect to a precipitation shaft, then it is possible to violate the Chebyshev condition, i.e., the near-surface reflectivity can become anti-correlated with the pencil-beam PIA. Given this complex behavior, how can precipitation retrieval algorithms accurately account for NUBF under all circumstances where it may occur?

In the TRMM PR radar profiling algorithm (Iguchi et al., 2009), an analytical solution to the NUBF problem is derived under the assumption that  $k_{ext}$  follows a gamma distribution within each range gate and that the nonuniformity is range-independent (perfectly correlated in the beam direction). This requires an estimate of the coefficient of variation,  $\sigma_n$ . Similarly, the GPM combined radar-radiometer algorithm subdivides a beam into components with lognormally-varying reflectivities, but this method requires an estimate of the variability as well. Universal estimates can be used, but these can introduce regional and seasonal biases since the scale of variability of precipitation is often storm-dependent (Tokay and Bashor, 2010). A desirable alternative is to use some local context, such as the convective/stratiform classification of the profile and the horizontal variability of SRT PIA estimates at the large scale, which can be used to inform the estimate of the local variability (Kozu and Iguchi 1999). Oversampling of the radar beam can produce finer-scale estimates of the SRT PIA that may be useful for this purpose as well (Takahashi et al., 2016). Since the SRT PIA is sensitive to NUBF, the probabilistic framework (18) can include a parameter describing the NUBF variability, which can aid in

fitting SRT PIA and multi-frequency radar measurements that cannot be easily explained with uniform beam filling.

## **[[H1]] Multiple Scattering**

Another phenomenon that can hinder the straightforward interpretation of radar reflectivity profiles is multiple scattering (MS). As the name suggests, this occurs when a sufficient amount of energy from the radar pulse undergoes multiple scattering events before returning to the receiver (Figure 14). Because the range of the scatterer to the radar is resolved via the time delay, echoes associated with MS enhances the reflectivity at range gates further from the radar than where the MS occurs (one indicator of MS is echo resolved below the surface). While MS is ubiquitous for radars with a finite beamwidth, it becomes important for the interpretation of radar measurements when the multiply-scattered signal becomes comparable to the single-scattered signal.

<<Figure 14: Schematic depiction of the multiple scattering process. The path of a multiple-scattered photon (black) is interpreted as echo from lower levels of the cloud following a single scattering event (red).>>

An extensive review of MS in the context of meteorological radars is given by Battaglia et al. (2010), and only a short summary is presented here focusing on 1) causes of MS, 2) simulations of MS, and 3) mitigation of MS in precipitation profiling algorithms. For the purposes of this section, “photon” refers to an infinitesimally small parcel of energy transmitted by the radar. Three properties of the radar system and scatterer (hydrometeors) are important in determining if MS will be significant:

1. Radar fields-of-view of comparable or larger size relative to the photon mean free path, which is inversely proportional to  $k_{ext}$ .
2. High single-scatter albedo, which increases the probability of a scattering event instead of an absorption event each time a photon interacts with the scatterer.
3. Phase functions that are peaked in the forward direction, keeping photons within the radar beam.

Analytical expressions quantifying MS have been derived by Kobayashi et al. (2005, 2007) for continuous wave and by Ito et al. (2007) for a time-dependent (pulse) wave. Hogan and Battaglia (2008) developed a computationally-efficient time-dependent two-stream approximation for plane-parallel atmospheres. Although computationally expensive, Monte Carlo simulations are well-suited to examining the MS problem by sampling the probabilities of scattering and absorption events within a three-dimensional scattering medium (Battaglia et al., 2005, 2006). To illustrate the effect of different radar parameters (frequency, beamwidth) under a large dynamic range of hydrometeor concentrations, Monte Carlo MS radar simulations were performed for a tropical mesoscale convective system simulated by the Weather Research and Forecasting model with 2-moment microphysics (Morrison et al., 2009) representing cloud water, cloud ice, snow, graupel, and rain (Figure 15).

<<Figure 15: Cross sections of water vapor mixing ratio ( $Q_v$ ), cloud water mixing ratio ( $Q_c$ ), rain mixing ratio ( $Q_r$ ) and number concentration ( $N_r$ ), graupel mixing ratio ( $Q_g$ ) and number concentration ( $N_g$ ), cloud ice mixing ratio ( $Q_i$ ) and number concentration ( $N_i$ ), and snow mixing ratio ( $Q_s$ ) and number concentration ( $N_s$ ) along a synthetic flight line over a WRF simulation of a tropical mesoscale convective system. The 0°C isotherm is indicated by the blue line. >>

Observations were simulated from a flight line that passed directly over a deep convective core as well as a broad stratiform anvil overspreading some shallow cumulus cells at Ku-, Ka-, and W-band from an altitude of 20km (Figure 16) and 400km (Figure 17) to represent high-altitude airborne and satellite observation, respectively. Both sets of simulations at all frequencies were assuming a 1-degree half-power beamwidth, which corresponds to a ground footprint size of 350m for the airborne simulation and 7 km for the satellite simulation. While this generally underestimates the beamwidth of airborne radars and overestimates the beamwidth of satellite-based radars presently in operation (Table 1), this is helpful for providing lower and upper bounds of expected MS effects from both vantage points. From the airborne perspective, MS enhancement is mostly limited to regions of extreme attenuation in the convective core between 50 and 100 km along track. Magnitudes vary from a few dB at Ku-band, 10-20 dB at Ka-band, to 30-40 dB at W-band. The stratiform region between 100 and 150 km, which contains significant amounts of ice aloft and little to no absorbing cloud water (resulting in high single-scatter albedo), also exhibits a few dB of MS enhancement at Ka-band and significant MS (> 10 dB) at W-band. From the satellite perspective, the wider beam width results in greater MS effects that reach to higher levels of the cloud than the airborne simulation. Significant echo that appears to be originating below the surface is also evident.

<<Figure 16: Nadir-viewing high-altitude airborne radar simulations of the tropical MCS in Figure 15 for a radar at 20km altitude with a 1-degree half-power Gaussian beamwidth. The top row shows single-scattering simulations at Ku-, Ka-, and W-band, the middle row shows Monte Carlo multiple-scattering simulations, and the bottom row shows the difference (multiple scattering enhancement) at each frequency. >>

<<Figure 17: Same as Figure 16 for a nadir-viewing satellite radar at 400km altitude with a 1-degree half-power Gaussian beamwidth. >>

For the retrieval framework (18), MS can be represented with a forward model that considers it, such as the Monte Carlo methods or Hogan and Battaglia (2008) plane-parallel model. Since it is evident from Figures 16 and 17 that MS does not significantly affect many profiles, it can be useful to first identify MS effects before invoking a computationally expensive forward model. Battaglia et al. (2014) argue that the differential slope ( $dZ_m/dh$ ) at a pair of frequencies should equal the differential attenuation plus the change in DFR that is mediated by changes in the PSD (Figure 9) with respect to height, which can be seen by combining equations (8) and (19):

$$DFR_m(r) = 10 \log_{10} \left( \frac{Z_{e,1}(r)}{Z_{e,2}(r)} \right) - 2 \int_0^r k_{ext,1}(s) - k_{ext,2}(s) ds. \quad (27)$$

Differentiating with respect to  $r$ ,

$$\frac{dDFR_m}{dr} = \frac{d(dBZ_{e,1} - dBZ_{e,2})}{dr} + 2 \left( k_{ext,2}(r) - k_{ext,1}(r) \right). \quad (28)$$

Because  $Z_e$  is often nearly constant with height, particularly below the melting layer, and attenuation increases predictably with frequency (Equation (6) and Figure 5), MS effects that reduce the differential slope to values that cannot be explained by any physical PSD can be a clear sign of multiple scattering that can “trigger” a MS-enabled forward model.

When the SRT PIA is used, MS effects must also be considered. If MS is weak compared to the surface return, it may safely be ignored. If MS is dominant, then there will be no peak in the surface return at the expected range gates (e.g., W-band in Figure 17), and SRT algorithms should be able to identify these cases and fail to provide a meaningful PIA value. However, when the MS effect is of comparable magnitude to the surface return, the result will be an

enhancement of  $\sigma_{0,R}$  that must be accounted for to avoid a low bias in the SRT PIA (Haynes et al., 2009).

## **[[H1]] Radar-Radiometer Methods**

Many times, airborne and spaceborne radars measurements are taken simultaneously with passive microwave measurements of the same scene. Passive microwave measurements can provide independent estimates of precipitation profiles (Evans et al., 1995, Kummerow et al., 1996) and, from a satellite perspective, can provide greatly enhanced coverage relative to radars (Hou et al., 2014). The placement of radar and radiometer on the same platform provides an opportunity for radiometer precipitation retrievals to be built from radar profiles (Kummerow et al., 2011, Kummerow et al., 2015). The radiometer measurements can also be used more directly to provide additional constraints to the radar profile (Haddad et al., 1997; Grecu et al., 2004; Munchak and Kummerow, 2011; Grecu et al., 2016). This section will provide a brief overview of the types of constraints that are provided by common frequencies on passive microwave instruments and how these can be integrated into the probabilistic retrieval framework (18).

The upwelling radiance measured by a passive microwave radiometer (commonly expressed in units of brightness temperature - Tb) is a complex function of processes along the radiometer line-of-sight described by the vector radiative transfer equation:

$$\frac{d\vec{I}(\hat{n}, \lambda)}{ds} = -\mathbf{K}\vec{I} + \bar{a}B(\lambda, T) + \int_{4\pi} \mathbf{Z}(\hat{n}, \hat{n}', \lambda) \vec{I} d\hat{n}' \quad (29)$$

which, in order of the terms on the right hand side, states that the radiance is reduced by extinction (absorption plus scattering), increased by emission (proportional to absorption) and increased by scattering into the path. In precipitation at microwave frequencies, none of these

terms can be ignored and the sensitivity of  $T_b$  to the PSD profile depends on whether absorption/emission (1<sup>st</sup> and 2<sup>nd</sup> term) or scattering (1<sup>st</sup> and 3<sup>rd</sup> term) is dominant and on the surface type, which determines the background against which the precipitation “signal” is superimposed (Munchak and Skofronick-Jackson, 2012). From Figures 4 and 5 it can be inferred that absorption is more important in the liquid phase, particularly at small size parameters, whereas scattering becomes dominant in the ice phase and at higher size parameters. The surface type plays a role because water surfaces are highly reflective, polarized, and to a good approximation, reflections can be treated as specular (Meissner and Wentz, 2012). Thus, at low frequencies, where absorption dominates, the  $T_b$  increases with the liquid water path (first row of Figure 18). Over land, which is less reflective, the emission from the surface is closer to the physical temperature of the surface and so the additional emission by hydrometeors in the atmosphere has little effect on  $T_b$  (second row of Figure 18). However, at higher frequencies, particularly when ice is present, extinction by scattering reduces the  $T_b$  significantly (lower right panels of Figure 18 and top left of Figure 19). Several radiative transfer models exist that can solve (27) under assumptions of a plane-parallel atmosphere (e.g., Wiscombe, 1977, Evans and Stephens, 1991, Heidinger et al., 2006) or for three-dimensional atmospheres (Evans 1998, Davis et al., 2005).

<<Figure 18: Two-dimensional histograms of radar-derived integrated liquid and ice water path and vertically-polarized observed brightness temperature from one day of GPM data at 10.65,18.7,36.64,89, and 166 GHz, separately for land and water surfaces. >>

In the framework of a radar retrieval, these models can be used to convert PSD profiles derived from single- or multi-frequency measurements to  $T_b$  at any frequency for which the hydrometeor scattering properties, absorption by atmospheric gases, and surface emissivity are known. The

problem then becomes one of how to represent the radiometer measurements in  $\mathbf{y}$  and  $f(\mathbf{x})$  in (18). If the radiometer line-of-sight and beamwidth are identical to the radar, the  $T_b$  in  $f(\mathbf{x})$  can be computed directly from the radar profile if three-dimensional effects are ignored. However, this is rarely the case, as passive microwave radiometers often have wider fields-of-view and are offset at an oblique angle (Figure 19) in order to take advantage of polarization differences that arise from surface and precipitation scattering (e.g., Prigent et al., 2005, Wang et al., 2012, Adams and Bettenhausen, 2012, Gong and Wu, 2017). One solution to this dilemma, and the one that is used by the GPM combined radar-radiometer algorithm (Greco et al., 2016), is deconvolution, which weights  $T_b$ s in an oversampled field in such a way as to achieve a common resolution while conserving the observed  $T_b$  (Petty and Bennartz, 2016) over the scene. Another option is to expand  $\mathbf{y}$  and  $\mathbf{x}$  to present observations and state variables describing multiple radar columns so that the slant path and native resolution radiometer observations can be more accurately modeled (Munchak and Kummerow, 2011), but since finding the minimum of (18) involves iterative matrix multiplication and inversion (Rogers et al., 2000), which scale as the third power of the length of  $\mathbf{y}$  and  $\mathbf{x}$ , this can be computationally expensive unless there are only a few state variables (e.g.,  $D_m$  at a few vertical levels) per radar column. Despite these challenges, the additional information provided by combining passive and active measurements of precipitation can better constrain surface properties such as wind over the ocean (Munchak et al., 2016) and precipitation profiles, particularly when ice is involved (Olson et al., 2016) than multi-frequency radar profiles alone.

<<Figure 19: Correlations between precipitation water content (PWC; left) or aggregate/pristine fraction (right) and 89/166 GHz brightness temperatures (top) and polarization difference (bottom) along a 53° slant path through an approximately uniform stratiform precipitation field.

These correlations were calculated from an ensemble of retrievals all consistent with measured Ku-band reflectivity profiles during the OLYMPEX field experiment on 3 December 2015.>>

## **[[H1]] Summary (1 page)**

The placement of weather radar on airborne and satellite platforms has proven to be of great utility for precipitation monitoring and the understanding of microphysical processes from sub-kilometer to global scales. While these platforms provide a unique vantage point from ground-based radars, they also present some challenges and limitations. The primary challenges for these platforms are limitations on weight, antenna size, and power consumption, all of which can be mitigated to some extent by the use of higher frequencies (Ku through W-band) than are typical for ground systems (S- or C-band). While these higher frequencies can provide sufficient sensitivity and angular resolution, they are much more prone to attenuation and multiple scattering, which respectively decrease and increase the measured reflectivity from that which is intrinsic to the precipitation PSD. A third phenomenon, non-uniform beam filling, can also cause departures in reflectivity from the uniform case and, like multiple scattering, its severity increases with the beamwidth.

In order to accurately retrieve the profile of precipitation PSD parameters from reflectivity profiles at one or more frequencies, optionally augmented by independent estimates of attenuation and/or passive microwave radiances, an optimal estimation framework has been described which minimizes a cost function consisting of normalized differences between observed and simulated measurements plus differences between the retrieved and *a priori* state vector. This framework is most robust when used with a forward model capable of simulating all aspects of the measurements that are relevant to the instrument, depending on frequency and

beamwidth (e.g., polarization, multiple scattering, non-uniform beam filling), and characterization of the PSD in the state vector using parameters that are uncorrelated to reflectivity.

As the capabilities of airborne and satellite-based radars continue to increase in the future, this framework can be used to understand new measurements as well as to critically evaluate the forward model. As an example of this iterative process, the inability of homogenous spherical models of ice to represent multi-frequency radar measurements led to advances in particle scattering models for realistically shaped crystals and crystal aggregates, and as these models become widely available they should be considered the standard for use in retrievals. It is by this iterative process that retrieval uncertainty becomes better-defined and is reduced by the additional of multiple, co-located measurements.

*Acknowledgments: Appreciation is extended to Ali Tokay (NASA GSFC/ University of Maryland, Baltimore County) for providing the Parsivel<sup>2</sup> data from IFloodS, Kwo-sen Kuo (NASA GSFC/University of Maryland, College Park) for the single scattering database of pristine and aggregate snow crystals, Ian Adams (Naval Research Laboratory) for the Monte Carlo multiple scattering model, and the APR3 team at NASA JPL for providing the data used in Figure 19. Appreciation is also extended to Dr. Robert Meneghini (NASA GSFC) and an anonymous reviewer for providing comments that improved the clarity and accuracy of this chapter.*

## [[H1]] References

- Adams, I. S. and Bettenhausen, M. H. (2012). The scattering properties of horizontally aligned snow crystals and crystal approximations at millimeter wavelengths. *Radio Science*, 47(5).
- Atlas, D. and Chmela, A. C. (1957). Physical-synoptic variations of raindrop size parameters. In *Proc. Sixth Weather Radar Conf* (pp. 21-29).
- Battaglia, A., M. O. Ajewole, and C. Simmer (2005), Multiple scattering effects due to hydrometeors on precipitation radar systems, *Geophys. Res. Lett.*, 32, L19801, doi:[10.1029/2005GL023810](https://doi.org/10.1029/2005GL023810).
- Battaglia, A., M. Ajewole, and C. Simmer, 2006: [Evaluation of Radar Multiple-Scattering Effects from a GPM Perspective. Part I: Model Description and Validation](#). *J. Appl. Meteor. Climatol.*, 45, 1634–1647, doi: 10.1175/JAM2424.1.
- Battaglia, A., Tanelli, S., Kobayashi, S., Zrnica, D., Hogan, R. J., & Simmer, C. (2010). Multiple-scattering in radar systems: A review. *Journal of Quantitative Spectroscopy and Radiative Transfer*, 111(6), 917–947.
- Battaglia, A., Tanelli, S., Heymsfield, G. M., & Tian, L. (2014). The dual wavelength ratio knee: A signature of multiple scattering in airborne Ku–Ka observations. *Journal of Applied Meteorology and Climatology*, 53(7), 1790-1808.
- Battaglia, A., Mroz, K., Lang, T., Tridon, F., Tanelli, S., Tian, L., & Heymsfield, G. M. (2016). Using a multiwavelength suite of microwave instruments to investigate the microphysical structure of deep convective cores. *Journal of Geophysical Research: Atmospheres*, 121(16), 9356-9381.
- Battan, L.J., 1973. Radar Observation of the Atmosphere. The University of Chicago Press, 324 pp.
- Beard, K. V., Bringi, V. N., and Thurai, M. (2010). A new understanding of raindrop shape. *Atmospheric research*, 97(4), 396-415.
- Behrangi, A., G. Stephens, R. Adler, G. Huffman, B. Lambriksen, and M. Lebsock, 2014: [An Update on the Oceanic Precipitation Rate and Its Zonal Distribution in Light of Advanced Observations from Space](#). *J. Climate*, 27, 3957–3965, doi: 10.1175/JCLI-D-13-00679.1.
- Boukabara, S. A., Garrett, K., Chen, W., Iturbide-Sanchez, F., Grassotti, C., Kongoli, C., ... & Ferraro, R. (2011). MiRS: An all-weather 1DVAR satellite data assimilation and retrieval system. *IEEE Transactions on Geoscience and Remote Sensing*, 49(9), 3249-3272.
- Brandes, E., G. Zhang, and J. Sun, 2006: [On the Influence of Assumed Drop Size Distribution Form on Radar-Retrieved Thunderstorm Microphysics](#). *J. Appl. Meteor. Climatol.*, 45, 259–268, doi: 10.1175/JAM2335.1.

Bringi, V. N., and V. Chandrasekar, 2001: *Polarimetric Doppler Weather Radar: Principles and Applications*. Cambridge University Press, 636 pp.

Bringi, V., L. Tolstoy, M. Thurai, and W. Petersen, 2015: [Estimation of Spatial Correlation of Drop Size Distribution Parameters and Rain Rate Using NASA's S-Band Polarimetric Radar and 2D Video Disdrometer Network: Two Case Studies from MC3E](#). *J. Hydrometeor.*, **16**, 1207–1221, doi: 10.1175/JHM-D-14-0204.1.

Chandrasekar, V., Schwaller, M., Vega, M., Carswell, J., Mishra, K. V., Meneghini, R., & Nguyen, C. (2010, July). Scientific and engineering overview of the NASA dual-frequency dual-polarized Doppler radar (D3R) system for GPM ground validation. In *Geoscience and Remote Sensing Symposium (IGARSS), 2010 IEEE International* (pp. 1308-1311). IEEE.

Davis, C., Emde, C., & Harwood, R. (2005). A 3-D polarized reversed Monte Carlo radiative transfer model for millimeter and submillimeter passive remote sensing in cloudy atmospheres. *IEEE transactions on geoscience and remote sensing*, *43*(5), 1096-1101.

Draine, B.T. and Flatau, P.J., "Discrete dipole approximation for scattering calculations", *J. Opt. Soc. Am. A*, *11*, 1491-1499 (1994)

Ellis, Scott M., and Jothiram Vivekanandan. "Water vapor estimates using simultaneous dual-wavelength radar observations." *Radio Science* 45.5 (2010).

Evans, K. F. and G. L. Stephens, 1991: A new polarized atmospheric radiative transfer model. *J. Quant. Spectrosc. Radiat. Transfer*, **46**, 412–423.

Evans, K. F., Turk, J., Wong, T., & Stephens, G. L. (1995). A Bayesian approach to microwave precipitation profile retrieval. *Journal of Applied Meteorology*, *34*(1), 260-279.

Evans, K. F. (1998). The spherical harmonics discrete ordinate method for three-dimensional atmospheric radiative transfer. *Journal of the Atmospheric Sciences*, *55*(3), 429-446.

Evensen, G., 2006: *Data Assimilation: The Ensemble Kalman Filter*. Springer, 280 pp.

Freilich, M. H., and B. A. Vanhoff, 2003: The relationship between winds, surface roughness, and radar backscatter at low incidence angles from TRMM Precipitation Radar measurements. *J. Atmos. Oceanic Technol.*, **20**, 549–562

Galloway, J., Pazmany, A., Mead, J., McIntosh, R. E., Leon, D., French, J., ... & Vali, G. (1997). Detection of ice hydrometeor alignment using an airborne W-band polarimetric radar. *Journal of Atmospheric and Oceanic Technology*, *14*(1), 3-12.

Gong, J. and Wu, D. L.: Microphysical properties of frozen particles inferred from Global Precipitation Measurement (GPM) Microwave Imager (GMI) polarimetric measurements, *Atmos.*

Chem. Phys., 17, 2741-2757, doi:10.5194/acp-17-2741-2017, 2017.

Greco, M., W. S. Olson, and E. N. Anagnostou, 2004: Retrieval of precipitation profiles from multiresolution, multifrequency active and passive microwave observations. *J. Appl. Meteor.*, **43**, 562–575

Greco, M. and W. Olson, 2008: [Precipitating Snow Retrievals from Combined Airborne Cloud Radar and Millimeter-Wave Radiometer Observations](#). *J. Appl. Meteor. Climatol.*, **47**, 1634–1650, doi: 10.1175/2007JAMC1728.1.

Greco, M., W. Olson, S. Munchak, S. Ringerud, L. Liao, Z. Haddad, B. Kelley, and S. McLaughlin, 2016: [The GPM Combined Algorithm](#). *J. Atmos. Oceanic Technol.*, **33**, 2225–2245, doi: 10.1175/JTECH-D-16-0019.1.

Haddad, Z. S., S. L. Durden, and E. Im, 1996: Parameterizing the raindrop size distribution. *J. Appl. Meteor.*, **35**, 3–13

Haddad, Z. S., E. A. Smith, C. D. Kummerow, T. Iguchi, M. R. Farrar, S. L. Durden, M. Alves, and W. S. Olson, 1997: The TRMM 'day-1' radar/radiometer combined rain-profiling algorithm. *J. Meteor. Soc. Japan*, **75**, 799–809

Hartmann, D., H. Hendon, and R. Houze, 1984: [Some Implications of the Mesoscale Circulations in Tropical Cloud Clusters for Large-Scale Dynamics and Climate](#). *J. Atmos. Sci.*, **41**, 113–121

Haynes, J. M., L'Ecuyer, T. S., Stephens, G. L., Miller, S. D., Mitrescu, C., Wood, N. B., & Tanelli, S. (2009). Rainfall retrieval over the ocean with spaceborne W-band radar. *Journal of Geophysical Research: Atmospheres*, **114**(D8).

Heidinger, A. K., O'Dell, C., Bennartz, R., & Greenwald, T. (2006). The successive-order-of-interaction radiative transfer model. Part I: Model development. *Journal of applied meteorology and climatology*, **45**(10), 1388-1402.

Heymsfield, G., L. Tian, L. Li, M. McLinden, and J. Cervantes, 2013: [Airborne Radar Observations of Severe Hailstorms: Implications for Future Spaceborne Radar](#). *J. Appl. Meteor. Climatol.*, **52**, 1851–1867, doi: 10.1175/JAMC-D-12-0144.1.

Hogan, R. and A. Battaglia, 2008: [Fast Lidar and Radar Multiple-Scattering Models. Part II: Wide-Angle Scattering Using the Time-Dependent Two-Stream Approximation](#). *J. Atmos. Sci.*, **65**, 3636–3651, doi: 10.1175/2008JAS2643.1.

Hoskins, B. and D. Karoly, 1981: [The Steady Linear Response of a Spherical Atmosphere to Thermal and Orographic Forcing](#). *J. Atmos. Sci.*, **38**, 1179–1196

Hou, A., R. Kakar, S. Neeck, A. Azarbarzin, C. Kummerow, M. Kojima, R. Oki, K. Nakamura, and T. Iguchi, 2014: [The Global Precipitation Measurement Mission](#). *Bull. Amer. Meteor. Soc.*, **95**, 701–

722, doi: 10.1175/BAMS-D-13-00164.1.

Iguchi, T., Kozu, T., Meneghini, R., Awaka, J., & Okamoto, K. I. (2000). Rain-profiling algorithm for the TRMM precipitation radar. *Journal of Applied Meteorology*, 39(12), 2038-2052.

Iguchi, T., KWIATKOWSKI, J., Meneghini, R., AWAKA, J., & OKAMOTO, K. I. (2009). Uncertainties in the rain profiling algorithm for the TRMM precipitation radar. *Journal of the Meteorological Society of Japan. Ser. II*, 87, 1-30.

Illingworth, A. J., Barker, H. W., Beljaars, A., Ceccaldi, M., Chepfer, H., Clerbaux, N., ... & Fukuda, S. (2015). The EarthCARE satellite: The next step forward in global measurements of clouds, aerosols, precipitation, and radiation. *Bulletin of the American Meteorological Society*, 96(8), 1311-1332.

Ito, S., S. Kobayashi, T. Oguchi (2007): Multiple scattering formulation of pulsed beam waves in hydrometeors and its application to millimeter wave weather radar, *IEEE Geosci Remote Sens Lett*, 4 (2007), pp. 13-17

Jameson, A. and A. Kostinski, 2001: [What is a Raindrop Size Distribution?](#). *Bull. Amer. Meteor. Soc.*, **82**, 1169–1177

Jameson, A., M. Larsen, and A. Kostinski, 2015: [On the Variability of Drop Size Distributions over Areas](#). *J. Atmos. Sci.*, **72**, 1386–1397, doi: 10.1175/JAS-D-14-0258.1

Johnson, B. T., Olson, W. S., and Skofronick-Jackson, G. (2016). The microwave properties of simulated melting precipitation particles: sensitivity to initial melting. *Atmospheric Measurement Techniques*, 9(1), 9-21.

Keigler, J. E., and L. Krawitz, 1960: Weather radar observation from an earth satellite. *J. Geophys. Res.*, **65**, 2973–2808.

Kneifel, S., A.von Lerber, J. Tiira, D. Moisseev, P. Kollias, and J. Leinonen (2015), Observed relations between snowfall microphysics and triple-frequency radar measurements. *J. Geophys. Res. Atmos.*, 120, 6034–6055. doi: [10.1002/2015JD023156](#).

Kneifel, S., Kollias, P., Battaglia, A., Leinonen, J., Maahn, M., Kalesse, H., & Tridon, F. (2016). First observations of triple-frequency radar Doppler spectra in snowfall: Interpretation and applications. *Geophysical Research Letters*.

Kobayashi, S., S. Tanelli, and E. Im (2005), Second-order multiple-scattering theory associated with backscattering enhancement for a millimeter wavelength weather radar with a finite beam width, *Radio Sci.*, 40, RS6015, doi:[10.1029/2004RS003219](#).

Kobayashi, S., T. Oguchi, S. Tanelli, and E. Im (2007), Backscattering enhancement on spheroid-shaped hydrometeors: Considerations in water and ice particles of uniform size and Marshall-Palmer distributed rains, *Radio Sci.*, 42, RS2001, doi:[10.1029/2006RS003503](#).

Kojima, M., and Coauthors, 2012: Dual-frequency precipitation radar (DPR) development on the global precipitation measurement (GPM) core observatory. *Earth Observing Missions and Sensors: Development, Implementation, and Characterization II*, H. Shimoda et al., Eds., International Society for Optical Engineering (SPIE Proceedings, Vol. 8528), 85281A, doi:[10.1117/12.976823](https://doi.org/10.1117/12.976823).

Kollias, P., Miller, M. A., Luke, E. P., Johnson, K. L., Clothiaux, E. E., Moran, K. P., Widener, K. B., and Albrecht, B. A.: The Atmospheric Radiation Measurement Program cloud profiling radars: Second-generation sampling strategies, processing, and cloud data products, *Journal of Atmospheric and Oceanic Technology*, 24, 1199–1214, 2007.

Kozu, T., & Iguchi, T. (1999). Nonuniform beamfilling correction for spaceborne radar rainfall measurement: Implications from TOGA COARE radar data analysis. *Journal of Atmospheric and Oceanic Technology*, 16(11), 1722-1735.

Kubota, T., Iguchi, T., Kojima, M., Liao, L., Masaki, T., Hanado, H., ... & Oki, R. (2016). A Statistical Method for Reducing Sidelobe Clutter for the Ku-Band Precipitation Radar on board the GPM Core Observatory. *Journal of Atmospheric and Oceanic Technology*, 33(7), 1413-1428.

Kulie, M., M. Hiley, R. Bennartz, S. Kneifel, and S. Tanelli, 2014: [Triple-Frequency Radar Reflectivity Signatures of Snow: Observations and Comparisons with Theoretical Ice Particle Scattering Models](#). *J. Appl. Meteor. Climatol.*, 53, 1080–1098, doi: 10.1175/JAMC-D-13-066.1.

Kummerow, C., Olson, W. S., & Giglio, L. (1996). A simplified scheme for obtaining precipitation and vertical hydrometeor profiles from passive microwave sensors. *IEEE Transactions on Geoscience and Remote Sensing*, 34(5), 1213-1232.

Kummerow, C. D., S. Ringerud, J. Crook, D. Randel, and W. Berg, 2011: An observationally generated a priori database for microwave rainfall retrievals. *J. Atmos. Oceanic Technol.*, 28, 113–130, doi:[10.1175/2010JTECHA1468.1](https://doi.org/10.1175/2010JTECHA1468.1).

Kummerow, C., D. Randel, M. Kulie, N. Wang, R. Ferraro, S. Joseph Munchak, and V. Petkovic, 2015: [The Evolution of the Goddard Profiling Algorithm to a Fully Parametric Scheme](#). *J. Atmos. Oceanic Technol.*, 32, 2265–2280, doi: 10.1175/JTECH-D-15-0039.1.

Kuo, K., E. Smith, Z. Haddad, E. Im, T. Iguchi, and A. Mugnai, 2004: [Mathematical–Physical Framework for Retrieval of Rain DSD Properties from Dual-Frequency Ku–Ka-Band Satellite Radar](#). *J. Atmos. Sci.*, 61, 2349–2369

Kuo, K., W. Olson, B. Johnson, M. Grecu, L. Tian, T. Clune, B. van Aartsen, A. Heymsfield, L. Liao, and R. Meneghini, 2016: [The Microwave Radiative Properties of Falling Snow Derived from Nonspherical Ice Particle Models. Part I: An Extensive Database of Simulated Pristine Crystals and Aggregate Particles, and Their Scattering Properties](#). *J. Appl. Meteor. Climatol.*, 55, 691–708, doi: 10.1175/JAMC-D-15-0130.1.

Le, M., & Chandrasekar, V. (2013). Hydrometeor profile characterization method for dual-frequency

precipitation radar onboard the GPM. *IEEE Transactions on Geoscience and Remote Sensing*, 51(6), 3648-3658.

Lebsock, M. D., & L'Ecuyer, T. S. (2011). The retrieval of warm rain from CloudSat. *Journal of Geophysical Research: Atmospheres*, 116(D20).

Lebsock, M. D., Suzuki, K., Millán, L. F., and Kalmus, P. M.: The feasibility of water vapor sounding of the cloudy boundary layer using a differential absorption radar technique, *Atmos. Meas. Tech.*, 8, 3631-3645, doi:10.5194/amt-8-3631-2015, 2015.

Leinonen, J., S. Kneifel, D. Moisseev, J. Tyynelä, S. Tanelli, and T. Nousiainen (2012), Evidence of nonspheroidal behavior in millimeter-wavelength radar observations of snowfall, *J. Geophys. Res.*, 117, D18205, doi:[10.1029/2012JD017680](https://doi.org/10.1029/2012JD017680).

Leinonen, J., & Szyrmer, W. (2015). Radar signatures of snowflake riming: A modeling study. *Earth and Space Science*, 2(8), 346-358.

Li, L., E. Im, S. L. Durden, and Z. S. Haddad, 2002: A surface wind model-based method to estimate rain-induced radar path attenuation over ocean. *J. Atmos. Oceanic Technol.*, 19, 658-672

Li, L., S. Sekelsky, S. Reising, C. Swift, S. Durden, G. Sadowy, S. Dinardo, F. Li, A. Huffman, G. Stephens, D. Babb, and H. Rosenberger, 2001: [Retrieval of Atmospheric Attenuation Using Combined Ground-Based and Airborne 95-GHz Cloud Radar Measurements](#). *J. Atmos. Oceanic Technol.*, 18, 1345-1353, doi: 10.1175/1520-0426(2001)018<1345:ROAAUC>2.0.CO;2.

Li, L., Heymsfield, G., Carswell, J., Schaubert, D., Creticos, J., & Vega, M. (2008, July). High-altitude imaging wind and rain airborne radar (HIWRAP). In *Geoscience and Remote Sensing Symposium, 2008. IGARSS 2008. IEEE International* (Vol. 3, pp. III-354). IEEE.

Liao, L., R. Meneghini, and A. Tokay, 2014: [Uncertainties of GPM DPR Rain Estimates Caused by DSD Parameterizations](#). *J. Appl. Meteor. Climatol.*, 53, 2524-2537, doi: 10.1175/JAMC-D-14-0003.1.

Liu, G., 2004: [Approximation of Single Scattering Properties of Ice and Snow Particles for High Microwave Frequencies](#). *J. Atmos. Sci.*, 61, 2441-2456, doi: 10.1175/1520-0469(2004)061<2441:AOSPO>2.0.CO;2.

Marshall, J. S., and Palmer, W. M. K. (1948). The distribution of raindrops with size. *Journal of meteorology*, 5(4), 165-166.

Marshall, J., R. Langille, and W. Palmer, 1947: [MEASUREMENT OF RAINFALL BY RADAR](#). *J. Meteor.*, 4, 186-192

Matthews, A. J., Hoskins, B. J. and Masutani, M. (2004), The global response to tropical heating in the Madden-Julian oscillation during the northern winter. *Q.J.R. Meteorol. Soc.*, 130: 1991-2011. doi:10.1256/qj.02.123

Meissner, T., & Wentz, F. J. (2012). The emissivity of the ocean surface between 6 and 90 GHz over a large range of wind speeds and earth incidence angles. *IEEE Transactions on Geoscience and Remote Sensing*, *50*(8), 3004-3026.

Meneghini, R., J. Eckerman, and D. Atlas, 1983: Determination of rain rate from a spaceborne radar using measurements of total attenuation. *IEEE Trans. Geosci. Remote Sens.*, **21**, 34–43.

Meneghini, R., T. Iguchi, T. Kozu, L. Liao, K. Okamoto, J. Jones, and J. Kwiatkowski, 2000: [Use of the Surface Reference Technique for Path Attenuation Estimates from the TRMM Precipitation Radar](#). *J. Appl. Meteor.*, **39**, 2053–2070

Meneghini, R., L. Liao, and L. Tian, 2005: [A Feasibility Study for Simultaneous Estimates of Water Vapor and Precipitation Parameters Using a Three-Frequency Radar](#). *J. Appl. Meteor.*, **44**, 1511–1525, doi: 10.1175/JAM2302.1.

Meneghini, R. and J. A. Jones, “Standard deviation of spatially averaged surface cross section data from the TRMM precipitation radar,” *IEEE Geosci. Remote Sens. Lett.*, vol. 8, no. 2, pp. 293–297, Mar. 2011.

Meneghini, R., L. Liao, S. Tanelli, and S. L. Durden, 2012: Assessment of the performance of a dual-frequency surface reference technique over ocean. *IEEE Trans. Geosci. Remote Sens.*, **50**, 2968–2977, doi:[10.1109/TGRS.2011.2180727](#)

Meneghini, R., H. Kim, L. Liao, J. Jones, and J. Kwiatkowski, 2015: [An Initial Assessment of the Surface Reference Technique Applied to Data from the Dual-Frequency Precipitation Radar \(DPR\) on the GPM Satellite](#). *J. Atmos. Oceanic Technol.*, **32**, 2281–2296, doi: 10.1175/JTECH-D-15-0044.1

Meneghini, R., & Kim, H. (2016). Minimizing the Standard Deviation of Spatially Averaged Surface Cross-Sectional Data From the Dual-Frequency Precipitation Radar. *IEEE Transactions on Geoscience and Remote Sensing*.

Mishchenko, M. I., & Travis, L. D. (1998). Capabilities and limitations of a current FORTRAN implementation of the T-matrix method for randomly oriented, rotationally symmetric scatterers. *Journal of Quantitative Spectroscopy and Radiative Transfer*, *60*(3), 309-324.

Mitrescu, C., T. L'Ecuyer, J. Haynes, S. Miller, and J. Turk, 2010: CloudSat precipitation profiling algorithm—Model description. *J. Appl. Meteor. Climatol.*, **49**, 991–1003, doi:[10.1175/2009JAMC2181.1](#).

Morrison, H., Thompson, G., & Tatarskii, V. (2009). Impact of cloud microphysics on the development of trailing stratiform precipitation in a simulated squall line: Comparison of one-and two-moment schemes. *Monthly Weather Review*, *137*(3), 991-1007.

Munchak, S. J., and A. Tokay, 2008: Retrieval of raindrop size distribution from simulated dual-frequency radar measurements. *J. Appl. Meteor. Climatol.*, **47**, 223–239, doi:[10.1175/2007JAMC1524.1](#)

- Munchak, S. and C. Kummerow, 2011: [A Modular Optimal Estimation Method for Combined Radar-Radiometer Precipitation Profiling](#). *J. Appl. Meteor. Climatol.*, **50**, 433–448, doi: 10.1175/2010JAMC2535.1
- Munchak, S. J., & Skofronick-Jackson, G. (2013). Evaluation of precipitation detection over various surfaces from passive microwave imagers and sounders. *Atmospheric Research*, *131*, 81-94.
- Munchak, S., R. Meneghini, M. Grecu, and W. Olson, 2016: [A Consistent Treatment of Microwave Emissivity and Radar Backscatter for Retrieval of Precipitation over Water Surfaces](#). *J. Atmos. Oceanic Technol.*, **33**, 215–229, doi: 10.1175/JTECH-D-15-0069.1.
- Okamoto, K., J. Awaka, K. Nakamura, T. Ihara, T. Manabe, and T. Kozu, 1988: A feasibility study of rain radar for the Tropical Rainfall Measuring Mission. *J. Comm. Res. Lab.*, **35**, 109–208.
- Olson, W. S., Tian, L., Grecu, M., Kuo, K. S., Johnson, B. T., Heymsfield, A. J., ... & Meneghini, R. (2016). The Microwave Radiative Properties of Falling Snow Derived from Nonspherical Ice Particle Models. Part II: Initial Testing Using Radar, Radiometer and In Situ Observations. *Journal of Applied Meteorology and Climatology*, *55*(3), 709-722.
- Pazmany, A. L., McIntosh, R. E., Kelly, R. D., & Vali, G. (1994). An airborne 95 GHz dual-polarized radar for cloud studies. *IEEE transactions on geoscience and remote sensing*, *32*(4), 731-739.
- Petty, G. and W. Huang, 2010: [Microwave Backscatter and Extinction by Soft Ice Spheres and Complex Snow Aggregates](#). *J. Atmos. Sci.*, **67**, 769–787, doi: 10.1175/2009JAS3146.1.
- Petty, G. and W. Huang, 2011: [The Modified Gamma Size Distribution Applied to Inhomogeneous and Nonspherical Particles: Key Relationships and Conversions](#). *J. Atmos. Sci.*, **68**, 1460–1473, doi: 10.1175/2011JAS3645.1.
- Petty, G. W. and Bennartz, R.: Field-of-view characteristics and resolution matching for the Global Precipitation Measurement (GPM) Microwave Imager (GMI), *Atmos. Meas. Tech. Discuss.*, doi:10.5194/amt-2016-275, in review, 2016
- Prigent, C., E. Defer, J. R. Pardo, C. Pearl, W. B. Rossow, and J.-P. Pinty (2005), Relations of polarized scattering signatures observed by the TRMM Microwave Instrument with electrical processes in cloud systems, *Geophys. Res. Lett.*, *32*, L04810, doi:[10.1029/2004GL022225](#).
- Puri, S., Stephen, H., & Ahmad, S. (2011). Relating TRMM precipitation radar land surface backscatter response to soil moisture in the southern United States. *Journal of Hydrology*, *402*(1), 115-125.
- Reinhart, B., H. Fuelberg, R. Blakeslee, D. Mach, A. Heymsfield, A. Bansemmer, S. Durden, S. Tanelli, G. Heymsfield, and B. Lambriksen, 2014: [Understanding the Relationships between Lightning, Cloud Microphysics, and Airborne Radar-Derived Storm Structure during Hurricane Karl \(2010\)](#). *Mon. Wea. Rev.*, **142**, 590–605, doi: 10.1175/MWR-D-13-00008.1.
- Rodgers, C. D., 2000: *Inverse Methods for Atmospheric Sounding: Theory and Practice*. World

Scientific, 238 pp.

Ryu, Y., J. Smith, M. Baeck, L. Cunha, E. Bou-Zeid, and W. Krajewski, 2016: [The Regional Water Cycle and Heavy Spring Rainfall in Iowa: Observational and Modeling Analyses from the IFloodS Campaign](#). *J. Hydrometeor.*, **17**, 2763–2784, doi: 10.1175/JHM-D-15-0174.1.

Sadowy, G. A., Berkun, A. C., Chun, W., Im, E., & Durden, S. L. (2003). Development of an advanced airborne precipitation radar.(Technical Feature). *Microwave Journal*, *46*(1), 84-93.

Seto, S., and T. Iguchi, 2007: Rainfall-induced changes in actual surface backscattering cross sections and effects on rain estimates by spaceborne precipitation radar. *J. Atmos. Oceanic Technol.*, **24**, 1693–1709, doi:[10.1175/JTECH2088.1](#).

Shepherd, A., Ivins, E. R., Geruo, A., Barletta, V. R., Bentley, M. J., Bettadpur, S., ... & Horwath, M. (2012). A reconciled estimate of ice-sheet mass balance. *Science*, *338*(6111), 1183-1189.

Shimizu, S., TAGAWA, T., IGUCHI, T., & Hirose, M. (2009). Evaluation of the effects of the orbit boost of the TRMM satellite on PR rain estimates. *Journal of the Meteorological Society of Japan. Ser. II*, *87*, 83-92.

Simpson, J., Adler, R. F., & North, G. R. (1988). A proposed tropical rainfall measuring mission (TRMM) satellite. *Bulletin of the American meteorological Society*, *69*(3), 278-295.

Stephen, H., Ahmad, S., Piechota, T. C., & Tang, C. (2010). Relating surface backscatter response from TRMM precipitation radar to soil moisture: results over a semi-arid region. *Hydrology and Earth System Sciences*, *14*(2), 193-204.

Stephens, G. L., Vane, D. G., Boain, R. J., Mace, G. G., Sassen, K., Wang, Z., ... & Miller, S. D. (2002). The CloudSat mission and the A-Train: A new dimension of space-based observations of clouds and precipitation. *Bulletin of the American Meteorological Society*, *83*(12), 1771-1790.

Takahashi, N., Hanado, H., Nakamura, K., Kanemaru, K., Nakagawa, K., Iguchi, T., ... & Yoshida, N. (2016). Overview of the End-of-Mission Observation Experiments of Precipitation Radar Onboard the Tropical Rainfall Measuring Mission Satellite. *IEEE Transactions on Geoscience and Remote Sensing*, *54*(6), 3450-3459.

Tanelli, S., S. L. Durden and E. Im, "Simultaneous measurements of ku- and ka-band sea surface cross sections by an airborne Radar," in *IEEE Geoscience and Remote Sensing Letters*, vol. 3, no. 3, pp. 359-363, July 2006.

doi: 10.1109/LGRS.2006.872929

Tanelli, S., Sacco, G. F., Durden, S. L., & Haddad, Z. S. (2012, November). Impact of non-uniform beam filling on spaceborne cloud and precipitation radar retrieval algorithms. In *SPIE Asia-Pacific Remote Sensing* (pp. 852308-852308). International Society for Optics and Photonics.

Testud, J., S. Oury, R. Black, P. Amayenc, and X. Dou, 2001: [The Concept of "Normalized" Distribution](#)

[to Describe Raindrop Spectra: A Tool for Cloud Physics and Cloud Remote Sensing](#). *J. Appl. Meteor.*, **40**, 1118–1140

Tokay, A., & Short, D. A. (1996). Evidence from tropical raindrop spectra of the origin of rain from stratiform versus convective clouds. *Journal of Applied Meteorology*, *35*(3), 355-371.

Tokay, A., & Bashor, P. G. (2010). An experimental study of small-scale variability of raindrop size distribution. *Journal of Applied Meteorology and Climatology*, *49*(11), 2348-2365.

Ulbrich, C. W., 1983: Natural variations in the analytical form of the raindrop size distribution. *J. Climate Appl. Meteor*, **22**, 1764–1775

Ulbrich, C. and D. Atlas, 1998: [Rainfall Microphysics and Radar Properties: Analysis Methods for Drop Size Spectra](#). *J. Appl. Meteor.*, **37**, 912–923

Wang, J.R., G. M. Skofronick-Jackson, M. R. Schwaller, C. M. Johnson, W. B. Monosmith and Z. Zhang, "Observations of Storm Signatures by the Recently Modified Conical Scanning Millimeter-Wave Imaging Radiometer," in *IEEE Transactions on Geoscience and Remote Sensing*, vol. 51, no. 1, pp. 411-424, Jan. 2013. doi: 10.1109/TGRS.2012.2200690

Williams, C., V. Bringi, L. Carey, V. Chandrasekar, P. Gatlin, Z. Haddad, R. Meneghini, S. Joseph Munchak, S. Nesbitt, W. Petersen, S. Tanelli, A. Tokay, A. Wilson, and D. Wolff, 2014: [Describing the Shape of Raindrop Size Distributions Using Uncorrelated Raindrop Mass Spectrum Parameters](#). *J. Appl. Meteor. Climatol.*, **53**, 1282–1296, doi: 10.1175/JAMC-D-13-076.1.

Williams, C., 2016: [Reflectivity and Liquid Water Content Vertical Decomposition Diagrams to Diagnose Vertical Evolution of Raindrop Size Distributions](#). *J. Atmos. Oceanic Technol.*, **33**, 579–595, doi: 10.1175/JTECH-D-15-0208.1.

Wiscombe, W., 1977: The delta-*M* method: Rapid yet accurate radiative flux calculations for strongly asymmetric phase functions. *J. Atmos. Sci.*, **34**, 1408–1422

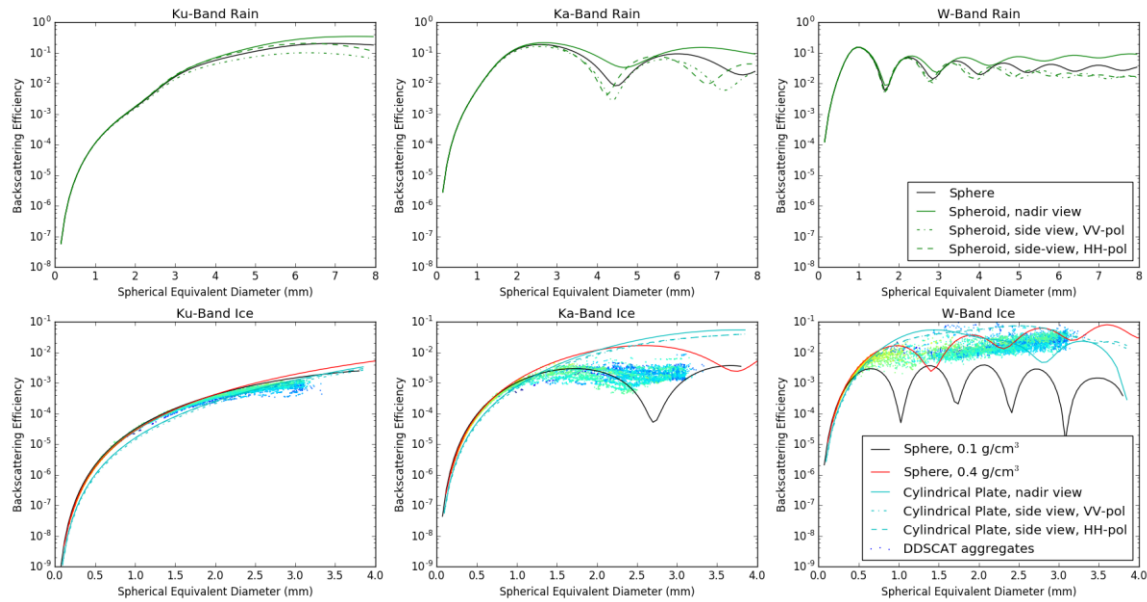
Zhang, G., J. Vivekanandan, E. A. Brandes, R. Meneghini, and T. Kozi, 2003: The shape–slope relation in observed gamma raindrop size distributions: Statistical error or useful information? *J. Atmos. Oceanic Technol.*, **20**, 1106–1119

<<Table 00-01>> Key parameters of spaceborne weather radars launched prior to 2016. The GPM DPR consists of two radars with matched beams: the KuPR and KaPR.

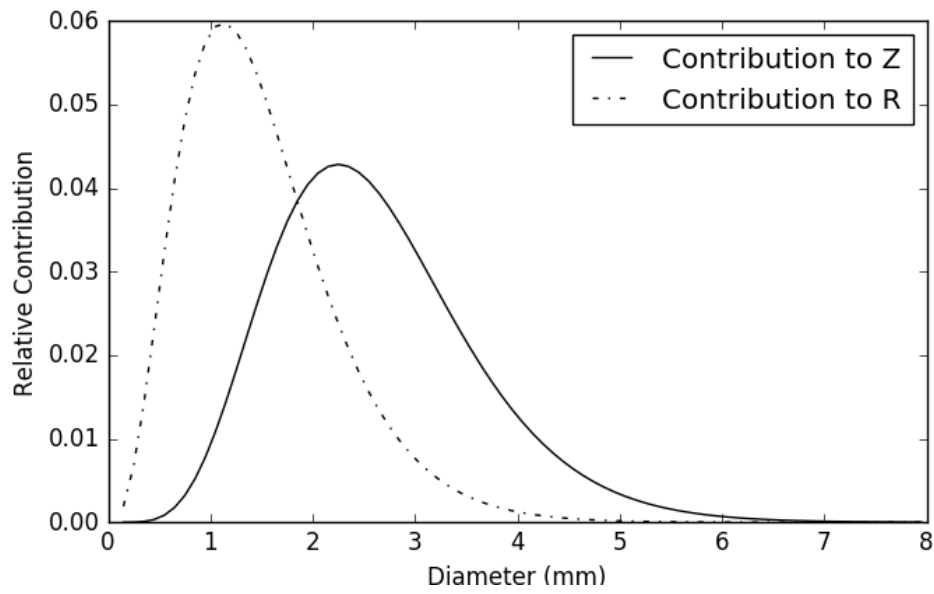
Name	Frequency	Half-power beamwidth & nominal ground footprint	Nominal altitude	Orbital Inclination	Vertical resolution	Minimum detectable signal
TRMM PR	13.8 GHz	0.71° 4.3 km (1997-2001) 5.0 km (2001-2014)	350 km (1997-2001) 402 km (2001-2014)	35°	250m	17 dBZ (1997-2001) 18 dBZ (2001-2014)
CloudSat CPR	94 GHz	0.108° 1.4 x 1.7 km	705 km	98.2°	480m	-30 dBZ (2006-2011)
GPM KuPR	13.6 GHz	0.71° 5 km	407 km	65°	250m	14 dBZ
GPM KaPR	35.55 GHz	0.71° 5 km	407 km	65°	250m (MS) 500m (HS)	18 dBZ (MS) 12 dBZ (HS)

<<Table 00-02>> Band designations, frequency ranges, and significant absorption lines in each band.

Designation	Frequency range (GHz)	Significant Gas Absorption lines
S	2-4	
C	4-8	
X	8-12	
Ku	12-18	
K	18-27	H <sub>2</sub> O (22.235 GHz)
Ka	27-40	
V	40-75	O <sub>2</sub> (several lines 49-70 GHz)
W	75-110	
G	110-300	O <sub>2</sub> (118.75 GHz), H <sub>2</sub> O (183.31 GHz)

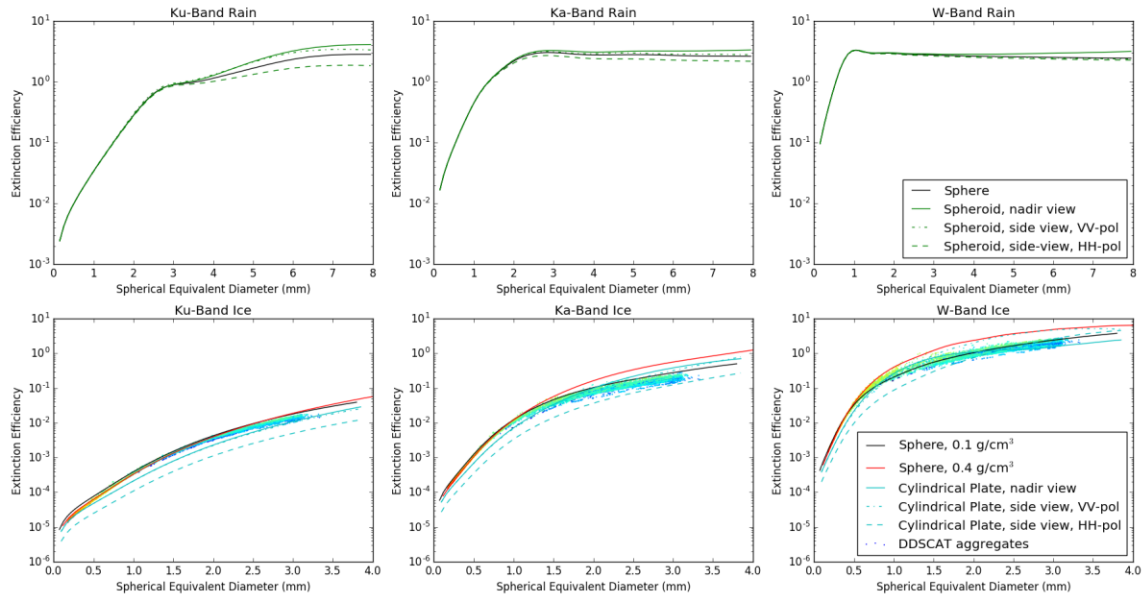


<<Figure 1: Backscattering efficiencies calculated at Ku-, Ka-, and W-band frequencies for rain and ice particles. Spheroidal raindrops were modeled according to aspect ratio and canting angle distributions given in Beard et al., 2010. The cylindrical snow particles, which are an effective representation of hexagonal plates (Adams et al., 2012), were modeled with an aspect ratio ( $D/h$ ) = 6 and effective density of  $0.6 \text{ g/cm}^3$ . The DDSCAT particles (color indicates relative density) are from the database of Kwo et al. (2016). >>

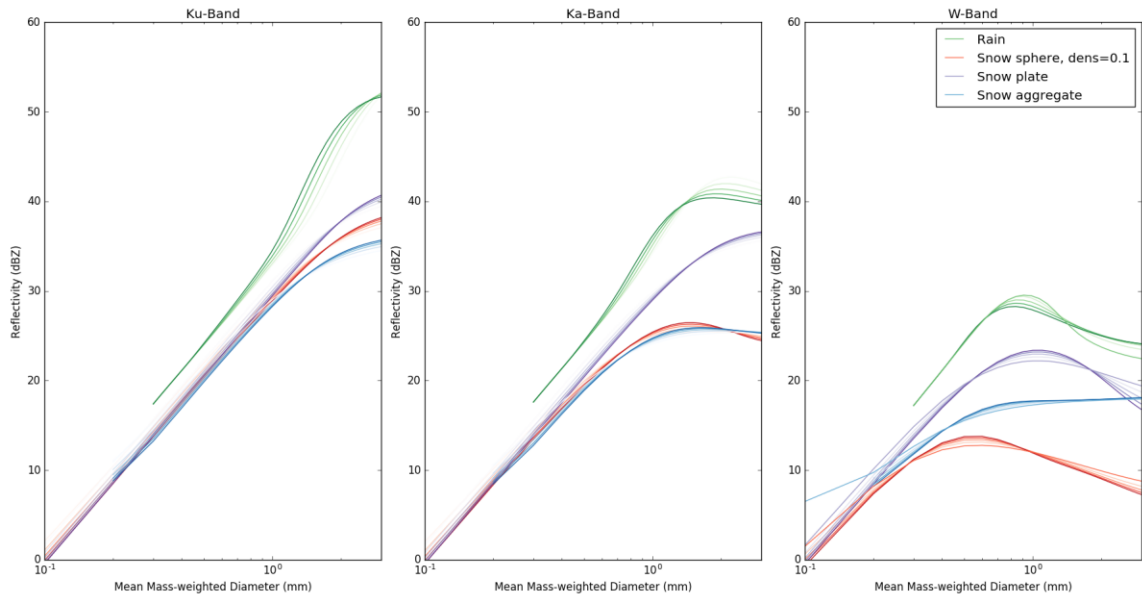


<<Figure 2:

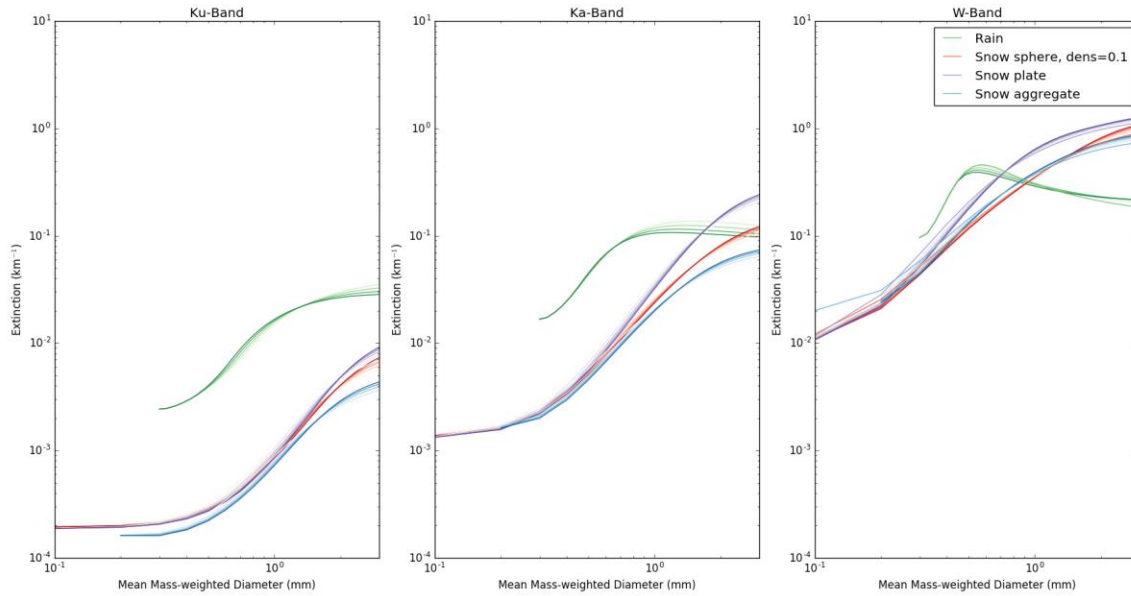
Relative contribution (in 0.1 mm bins) to reflectivity (Z) and rainfall rate (R) of an exponential drop size distribution with a median volume-weighted diameter of 1.5 mm. >>



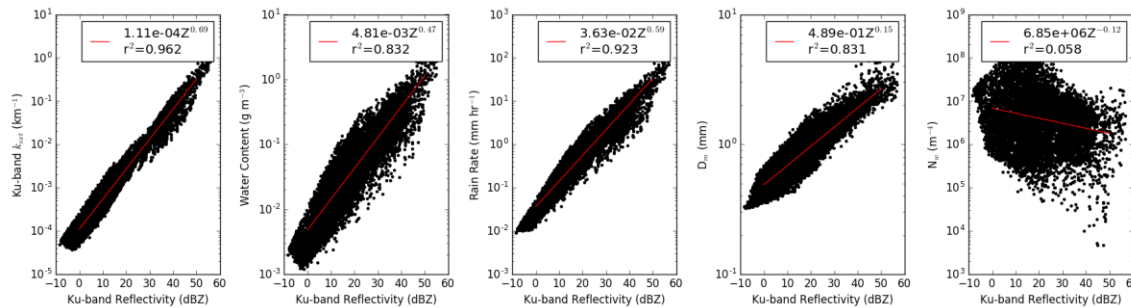
<<Figure 3: Extinction efficiencies calculated at Ku-, Ka-, and W-band frequencies for rain and ice particles. Particle type description can be found in the Figure 1 caption.>>



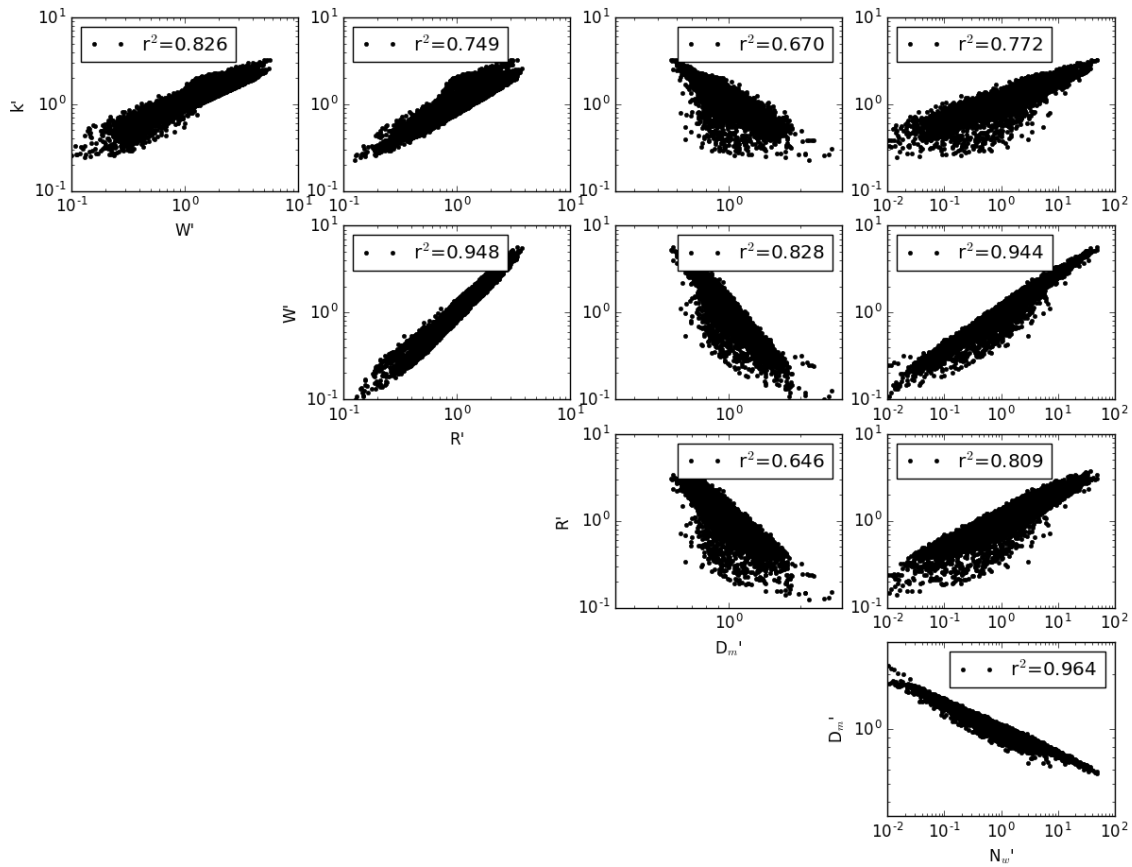
<<Figure 4: Reflectivity for rain and ice PSDs at Ku-, Ka-, and W-band as a function of mass-weighted mean particle diameter  $D_m$  for various shape parameter assumptions. All PSDs contain 1 g m<sup>-3</sup> of water content.>>



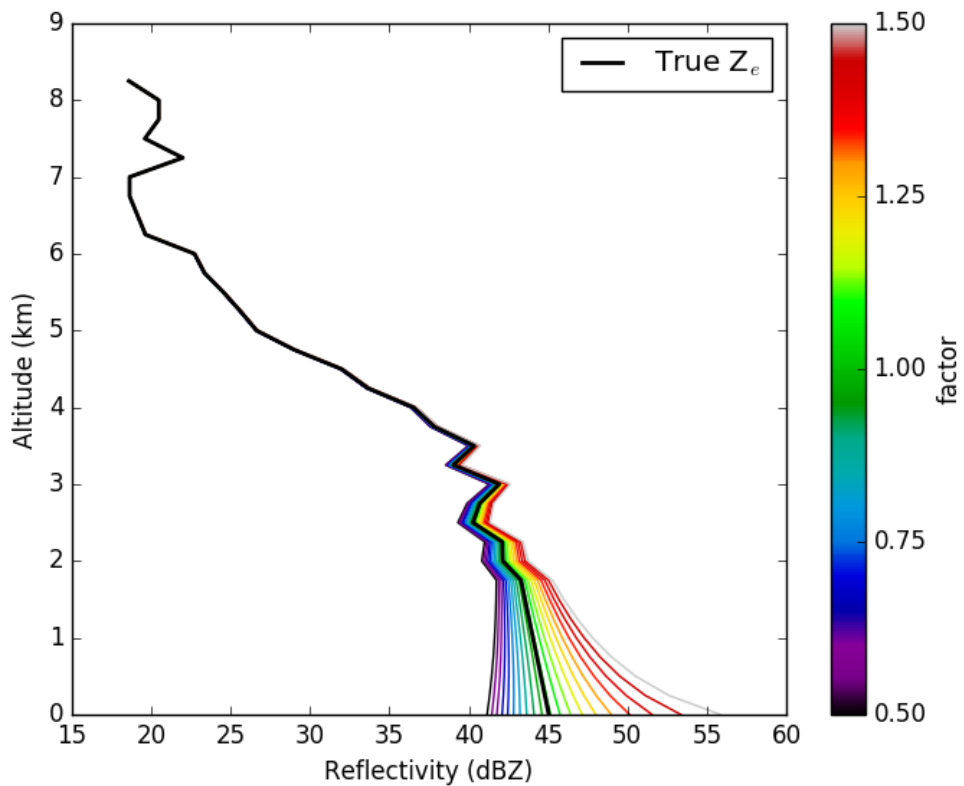
<<Figure 5: Bulk extinction coefficient at Ku-, Ka-, and W-band for the same PSDs represented in Figure 4.>>



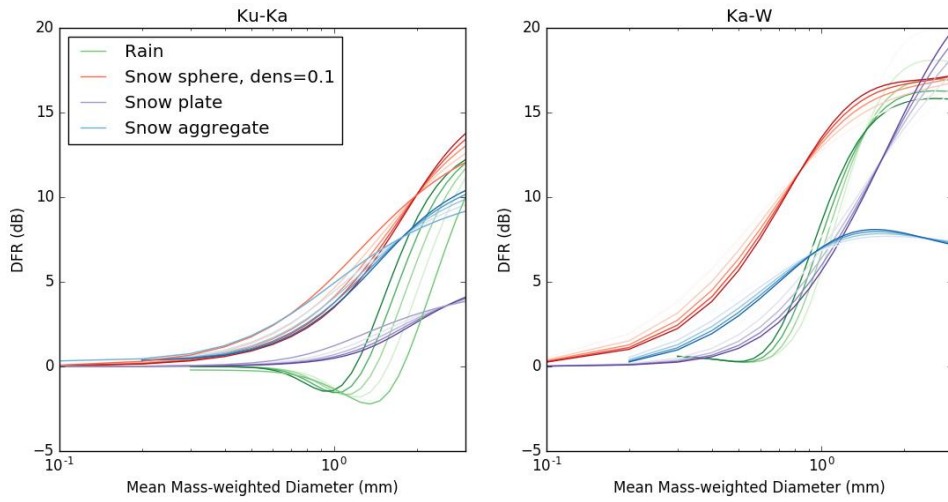
<<Figure 6: Ku-band reflectivity power laws and squared correlation coefficient derived from Parsivel<sup>2</sup> disdrometer measurements in Iowa during the IFloodS field experiment for the integral parameters: attenuation coefficient at Ku-band ( $k_{ext}$ ), liquid water content ( $W$ ), rain rate ( $R$ ), mean mass-weighted diameter ( $D_m$ ), and normalized intercept parameter ( $N_w$ ). >>



<<Figure 7: Scatter diagrams for pairs of normalized integral quantities (equation 14) from the IFloodS disdrometer measurements. The squared logarithmic correlation coefficient is labeled in each panel. >>

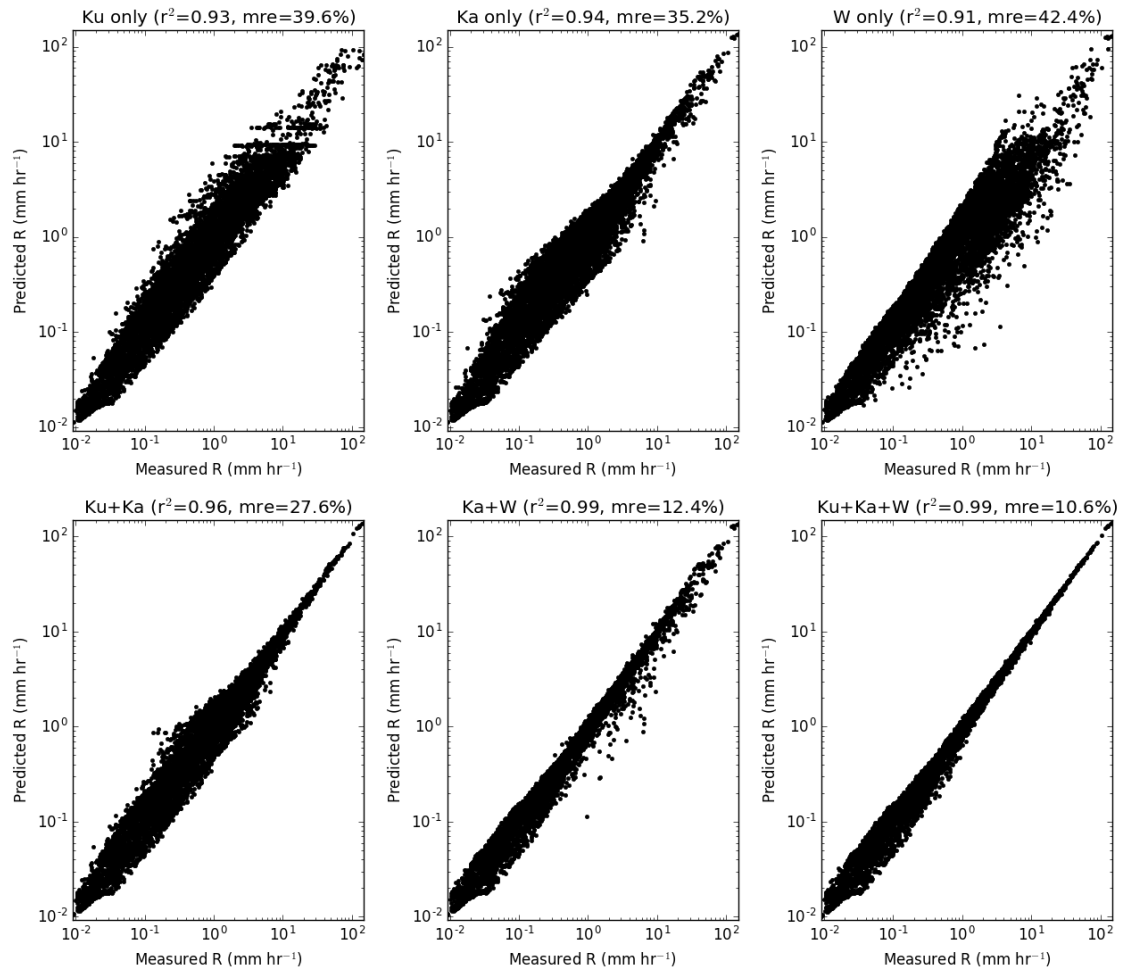


<<Figure 8: An example attenuation-correcting radar profiling algorithm. The true effective reflectivity (solid) is attenuated to the measured signal (dashed). An attenuation correction is applied assuming  $Z-k_{ext}$  relationships that are have been multiplied by factors ranging from 0.5 to 1.5.>>

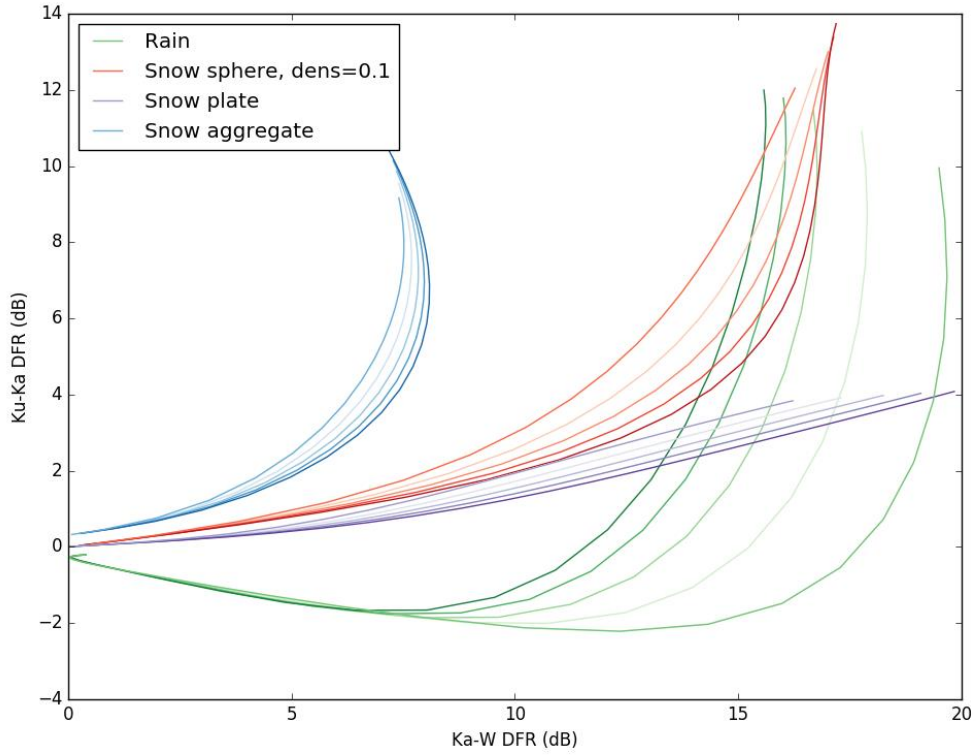


<<Figure 9: Dual-frequency ratio vs.  $D_m$  for Ku-Ka (left) and Ka-W (right) frequency pairs.

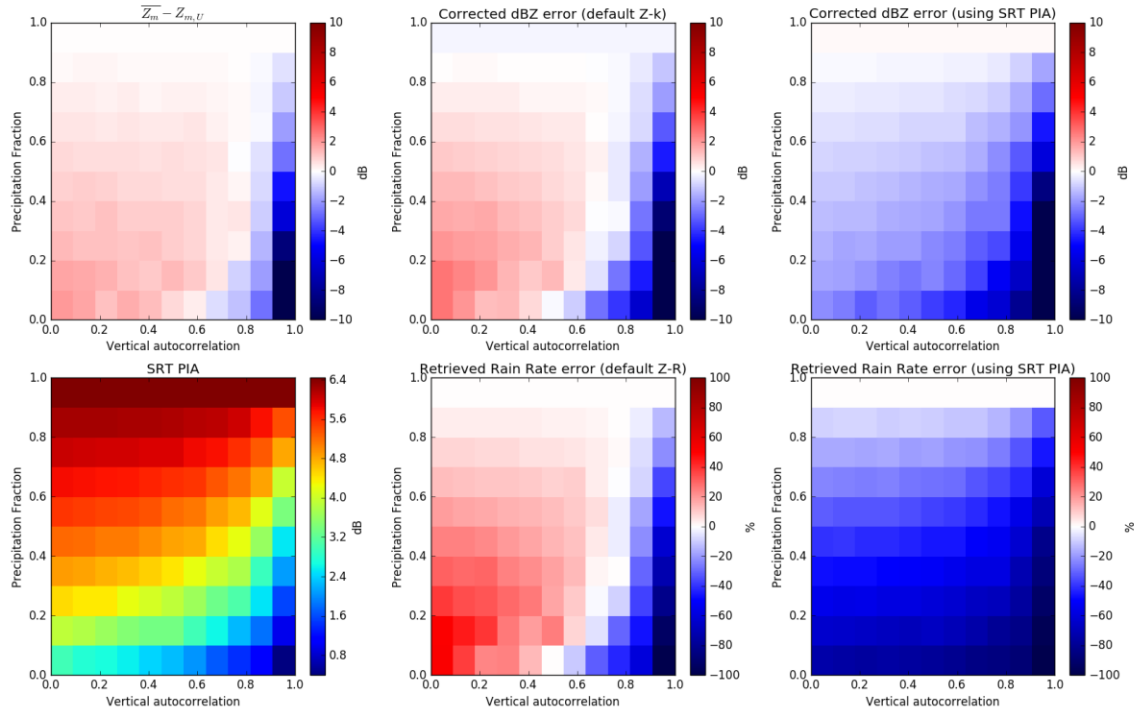
Different values for  $\mu$  (ice) or  $\sigma_m'$  (rain) are indicated by different shades of each color, as in Figures 4 and 5.>>



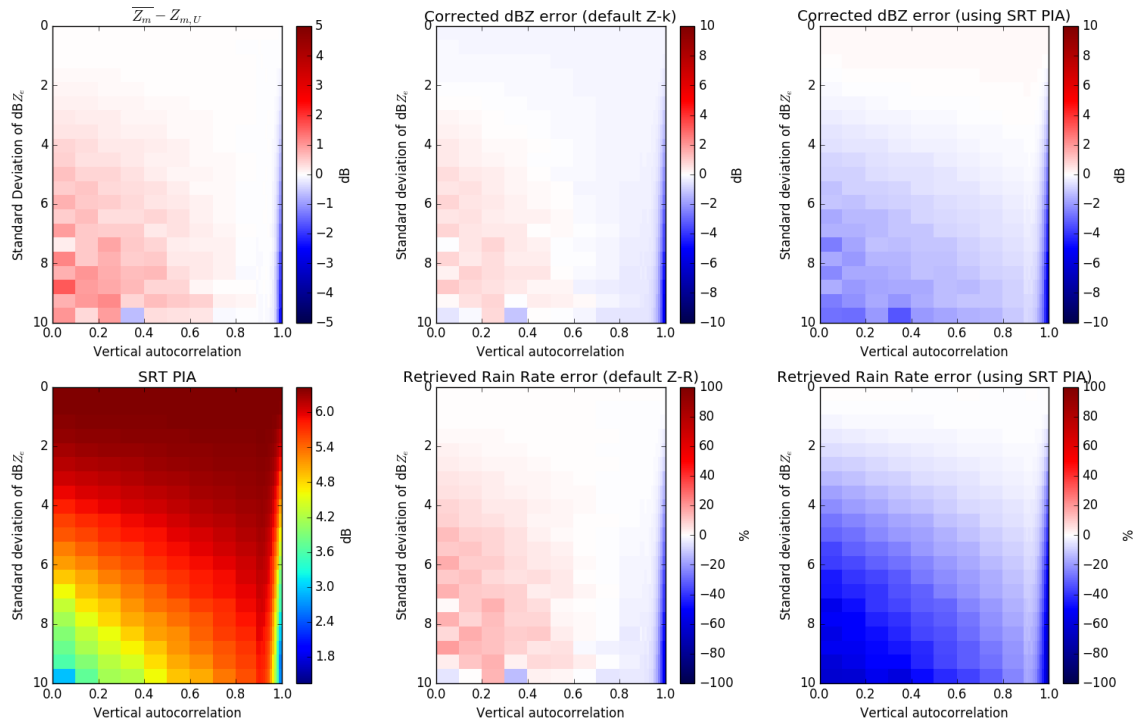
<<Figure 10: Observed vs. predicted rainfall rate from equation (20) from the IFloodS PSD database for different combinations of Ku, Ka, and W-band reflectivity measurements, assuming a perfect attenuation correction is made and 1 dB measurement error. The squared correlation coefficient ( $r^2$ ) and mean relative error (mre) are given for each combination.>>



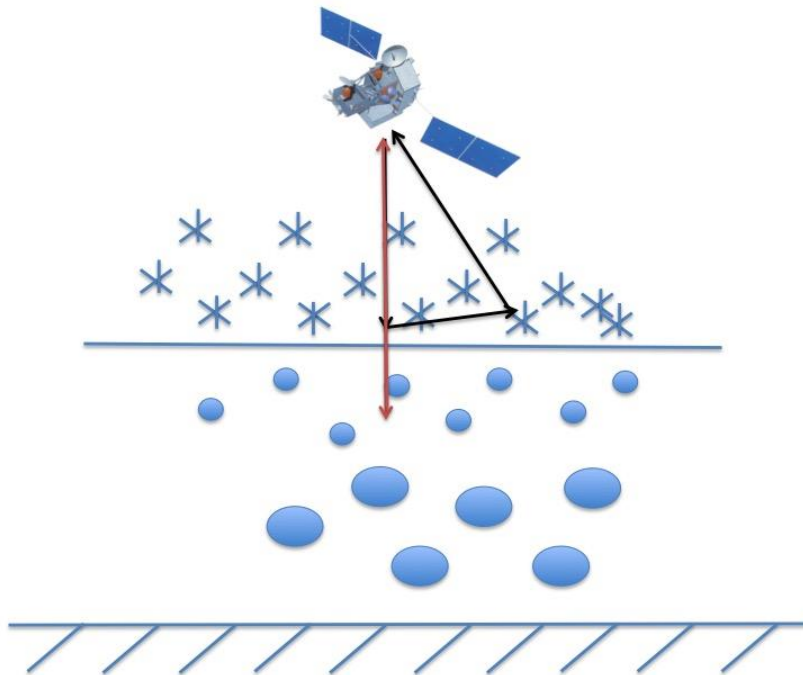
<<Figure 11: Dual-frequency ratio at Ka and W bands vs. dual-frequency ratio at Ku-Ka bands for the hydrometeor PSDs used in Figures 4,5, and 9.>>



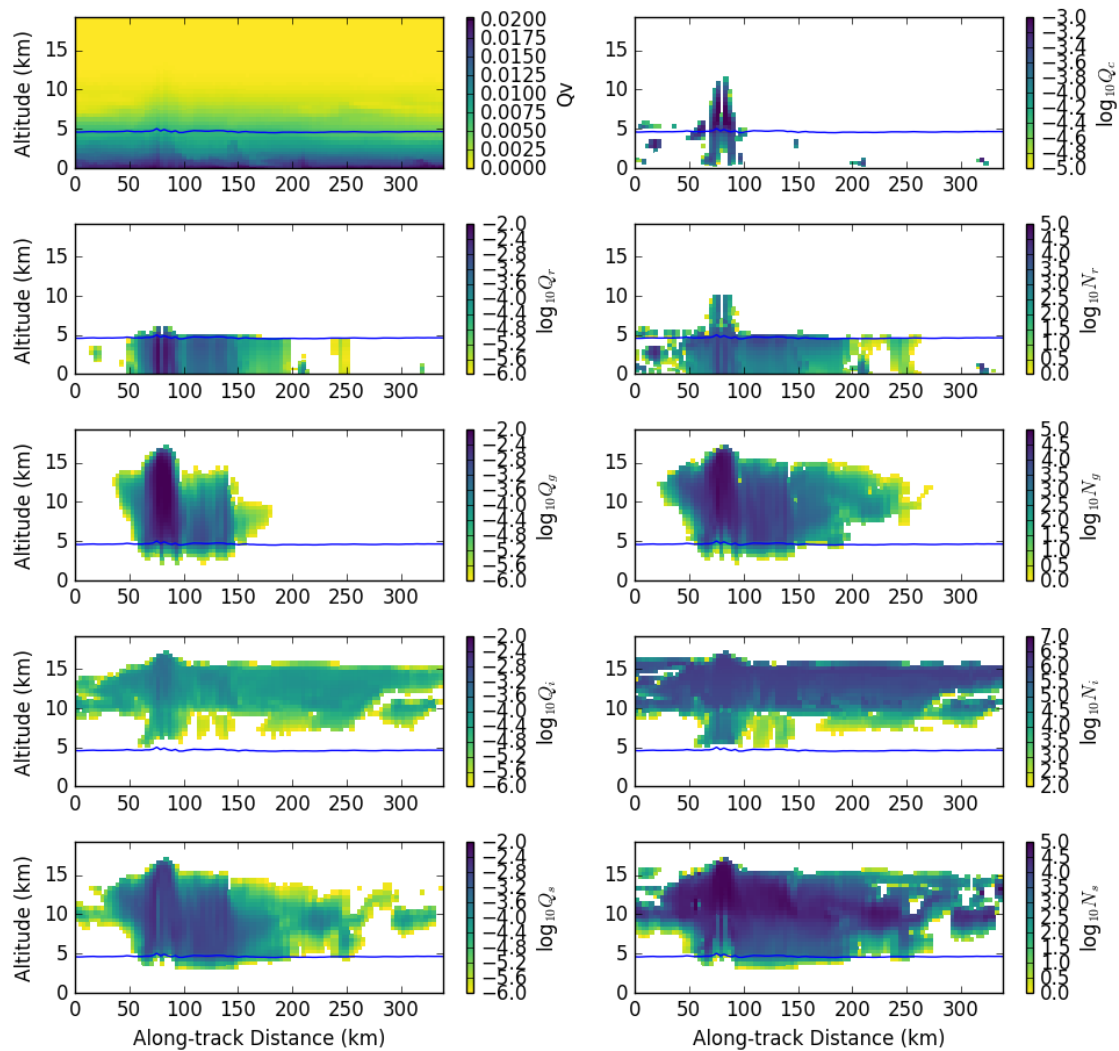
<<Figure 12: Non-uniform beam filling scenarios for the  $Z_e$  profile presented in Figure 8. These scenarios vary the fraction of the beam containing precipitation at each level on the vertical axis and the autocorrelation of precipitation from one vertical level to the next on the horizontal axis. In these scenarios, the precipitation is uniform where present and scaled such that the average non-attenuated reflectivity is constant at each level. The difference in measured reflectivity from a uniform beam, SRT PIA, and errors in corrected reflectivity and retrieved rainfall rate near the surface (using default relationships and the SRT PIA to adjust the PSD) are shown.>>



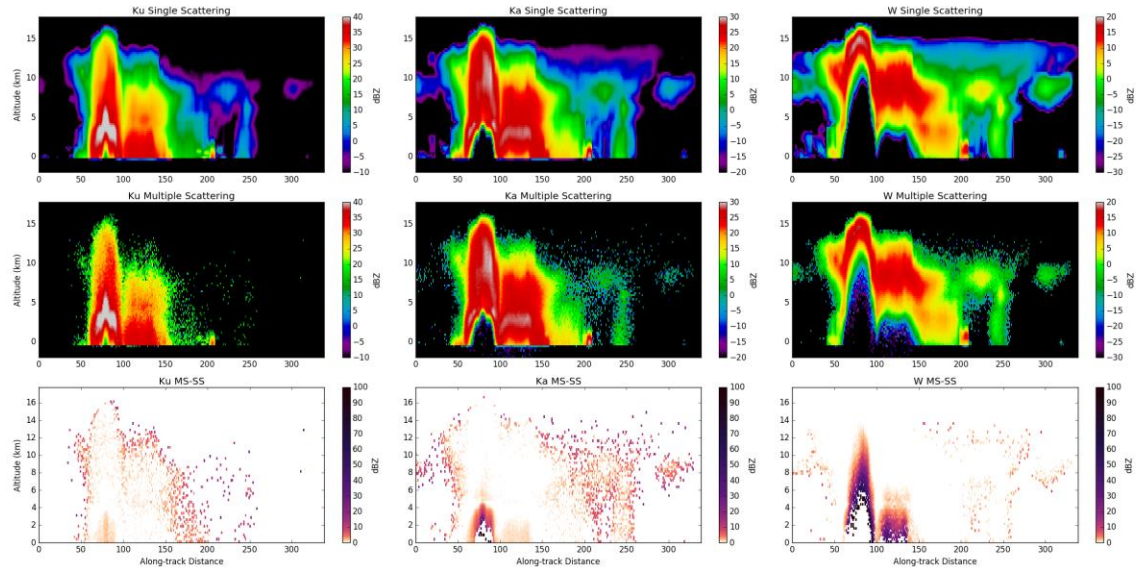
<<Figure 13: Non-uniform beam filling scenarios for the  $Z_e$  profile presented in Figure 8. These scenarios vary the standard deviation of  $dBZ_e$  at each level (scaled such that the average non-attenuated reflectivity is unmodified from the original profile) on the vertical axis and the autocorrelation of precipitation from one vertical level to the next on the horizontal axis. The difference in measured reflectivity from a uniform beam, SRT PIA, and errors in corrected reflectivity and retrieved rainfall rate near the surface (using default relationships and the SRT PIA to adjust the PSD) are shown.>>



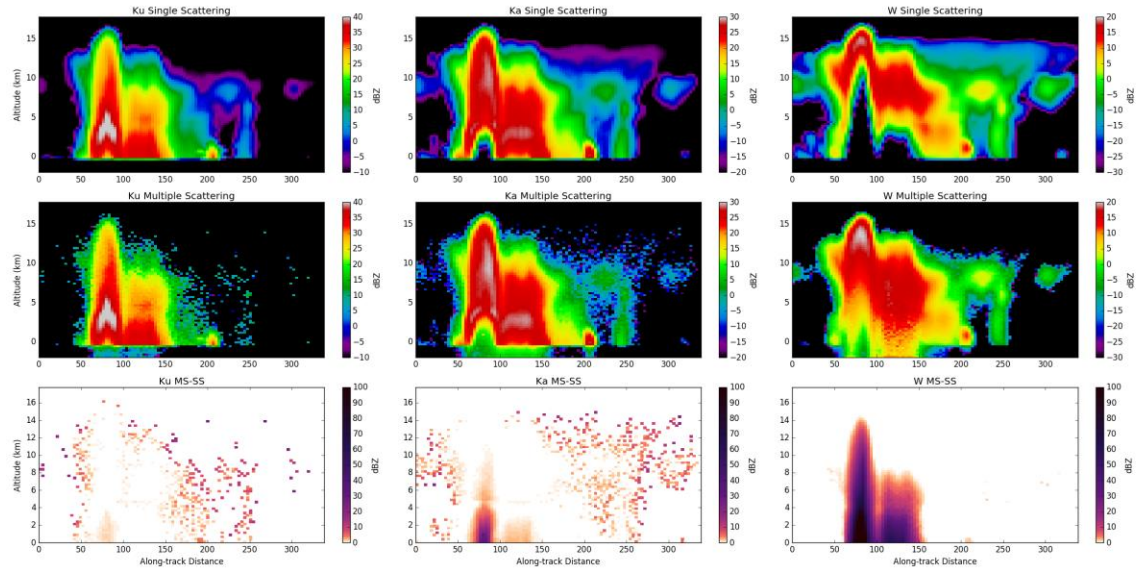
<<Figure 14: Schematic depiction of the multiple scattering process. The path of a multiple-scattered photon (black) is interpreted as echo from lower levels of the cloud following a single scattering event (red).>>



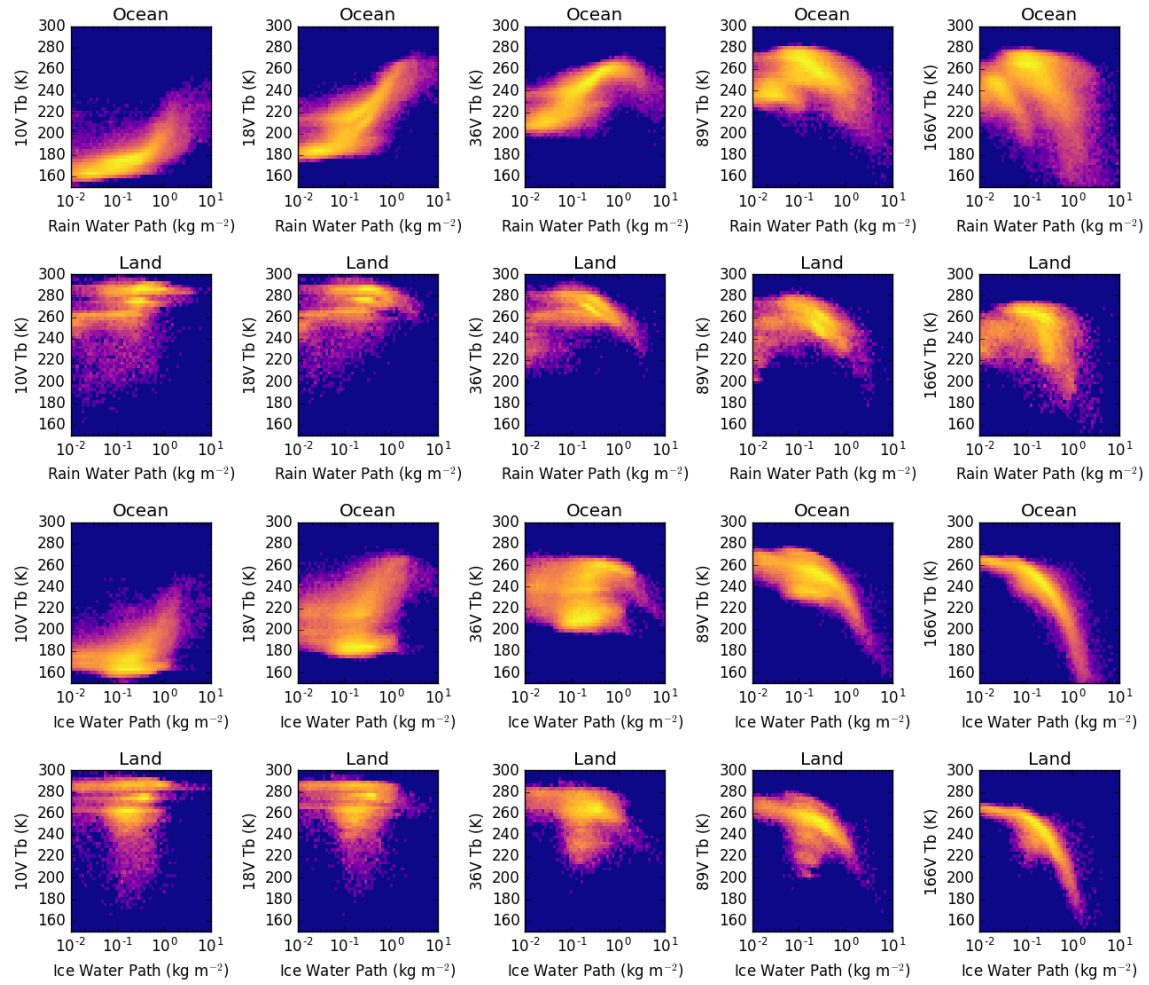
<<Figure 15: Cross sections of water vapor mixing ratio ( $Q_v$ ), cloud water mixing ratio ( $Q_c$ ), rain mixing ratio ( $Q_r$ ) and number concentration ( $N_r$ ), graupel mixing ratio ( $Q_g$ ) and number concentration ( $N_g$ ), cloud ice mixing ratio ( $Q_i$ ) and number concentration ( $N_i$ ), and snow mixing ratio ( $Q_s$ ) and number concentration ( $N_s$ ) along a synthetic flight line over a WRF simulation of a tropical mesoscale convective system. The 0°C isotherm is indicated by the blue line. >>



<<Figure 16: Nadir-viewing high-altitude airborne radar simulations of the tropical MCS in Figure 15 for a radar at 20km altitude with a 1-degree half-power Gaussian beamwidth. The top row shows single-scattering simulations at Ku-, Ka-, and W-band, the middle row shows Monte Carlo multiple-scattering simulations, and the bottom row shows the difference (multiple scattering enhancement) at each frequency. >>

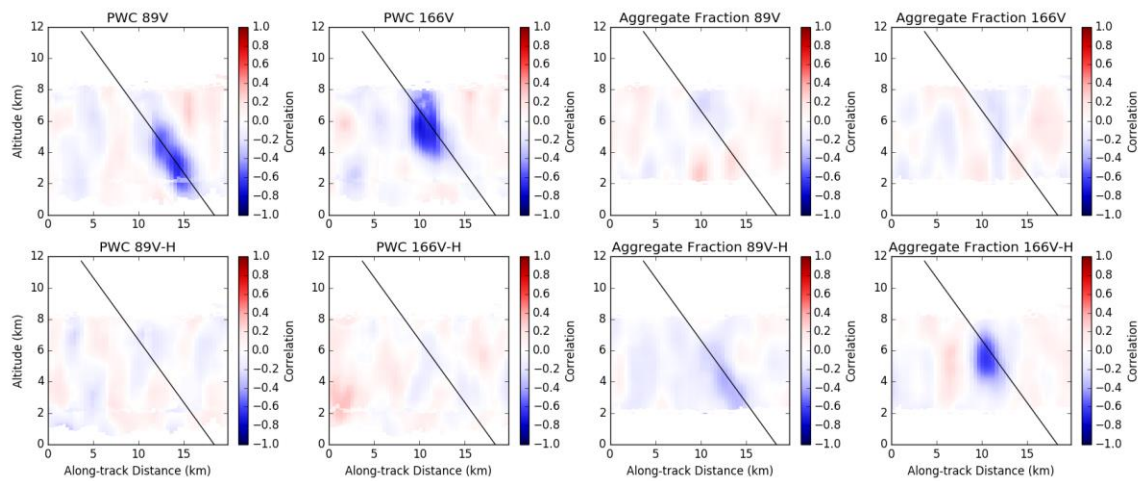


<<Figure 17: Same as Figure 16 for a nadir-viewing satellite radar at 400km altitude with a 1-degree half-power Gaussian beamwidth. >>



<<Figure 18: Two-dimensional histograms of radar-derived integrated liquid and ice water path and vertically-polarized observed brightness temperature from one day of GPM data at

10.65,18.7,36.64,89, and 166 GHz, separately for land and water surfaces. >>



<<Figure 19: Correlations between precipitation water content (PWC; left) or aggregate/pristine fraction (right) and 89/166 GHz brightness temperatures (top) and polarization difference (bottom) along a  $53^\circ$  slant path through an approximately uniform stratiform precipitation field. These correlations were calculated from an ensemble of retrievals all consistent with measured Ku-band reflectivity profiles during the OLYMPEX field experiment on 3 December 2015.>>